




Hyperbolic Topological Band Insulators

David M. Urwyler,¹ Patrick M. Lenggenhager ^{1,2,3} Igor Boettcher ^{4,5}
 Ronny Thomale ⁶ Titus Neupert ¹ and Tomáš Bzdušek ^{2,1,*}

¹Department of Physics, University of Zurich, Winterthurerstrasse 190, 8057 Zurich, Switzerland

²Condensed Matter Theory Group, Paul Scherrer Institute, 5232 Villigen PSI, Switzerland

³Institute for Theoretical Physics, ETH Zurich, 8093 Zurich, Switzerland

⁴Department of Physics, University of Alberta, Edmonton, Alberta T6G 2E1, Canada

⁵Theoretical Physics Institute, University of Alberta, Edmonton, Alberta T6G 2E1, Canada

⁶Institut für Theoretische Physik und Astrophysik, Universität Würzburg, 97074 Würzburg, Germany

(Dated: January 10, 2023)

Recently, hyperbolic lattices that tile the negatively curved hyperbolic plane emerged as a new paradigm of synthetic matter, and their energy levels were characterized by a band structure in a four- (or higher-)dimensional momentum space. To explore the uncharted topological aspects arising in hyperbolic band theory, we here introduce elementary models of hyperbolic topological band insulators: the hyperbolic Haldane model and the hyperbolic Kane-Mele model; both obtained by replacing the hexagonal cells of their Euclidean counterparts by octagons. Their non-trivial topology is revealed by computing topological invariants in both position and momentum space. The bulk-boundary correspondence is evidenced by comparing bulk and boundary density of states, by modelling propagation of edge excitations, and by their robustness against disorder.

Introduction.—The interplay between the crystal structure of materials and their electronic band-structure topology is pivotal to modern condensed matter physics, with major recent developments in areas such as topological quantum chemistry [1–3] and moiré materials [4]. With the groundbreaking experimental realization of hyperbolic lattices in coupled waveguide resonators [5] and electric-circuit networks [6], such exotic lattices have been elevated from purely mathematical objects [7, 8] to promising tabletop platforms for simulating quantum many-body physics in curved space. These experimental achievements have also inspired numerous theoretical studies of hyperbolic lattices. Notably, hyperbolic band theory (HBT) has been formulated [9], enabling the characterization of their energy spectra via band structures in momentum space. The range of recently investigated physical phenomena further includes the effects of magnetic fields [10–12], continuum approximation [13], periodic boundary conditions [14–16], hyperbolic crystallography [17], photon bound states [18], exact trace formulas [19], Bose-Hubbard model [15], elastic vibrations [20], and flat bands [21–24]. Notably, two very recent works proposed concrete models of hyperbolic topological insulators [25, 26]; however, a systematic investigation of topological quantum numbers on hyperbolic lattices remains largely unexplored.

Among the multitude of hyperbolic lattices, which are tessellations of the two-dimensional (2D) hyperbolic plane of negative curvature [27], the so-called $\{8, 3\}$ lattice presents a unique opportunity for a first systematic study of band topology in toy models with topological ground states. The graph of this lattice consists of regular octagons with three lines meeting at each vertex. Hence it derives from the honeycomb lattice (denoted $\{6, 3\}$ in this context) through replacing hexagons by octagons. Importantly, HBT predicts that the Brillouin zone (BZ) of this lattice is four-dimensional

(4D) [17], with crystal momentum $\mathbf{k} = (k_1, k_2, k_3, k_4)$, separating the dimensions of position and momentum space as a genuine property of hyperbolic lattices. This enhanced dimensionality suggests [28, 29] that hyperbolic models may host larger families of strong and weak topological band insulators than their Euclidean counterparts.

In this Letter, we introduce two elemental models of hyperbolic topological band insulators, the hyperbolic Haldane and hyperbolic Kane-Mele (KM) models on the $\{8, 3\}$ lattice, which generalize the quintessential namesake Euclidean models formulated on the $\{6, 3\}$ lattice [30–34]. These models could be implemented experimentally using the platforms of Refs. 5, 6, 35–37. Importantly, due to the applicability of both HBT and real-space topological markers [38–42] on the $\{8, 3\}$ lattice, we are able to study band-topological properties in both position and momentum space. This dual point of view allows us to compare topological invariants of hyperbolic topological insulators in momentum and position space, and to study their associated bulk-boundary correspondence. Our models and analysis surpass the study of hyperbolic Hofstadter and Haldane-like models in Refs. 10, 25, and 26 as they do not utilize the complementary momentum-space picture.

Tight-binding models.—We consider models on the hyperbolic $\{8, 3\}$ lattice, which is comprised of octagonal faces with three lines meeting at each vertex, see Fig. 1a. This lattice consists of a 16-site unit cell that is repeated infinitely many times according to a hyperbolic Bravais lattice, which is the $\{8, 8\}$ lattice in this case [17], comprised of octagonal plaquettes with coordination number eight. We refer to the unit cell as the *Bolza cell* – a name inspired by the fact that this cell covers the Bolza surface (the most symmetric genus-two Riemann surface [43]). The Bravais lattice is generated by four non-commuting hyperbolic translations, denoted $\gamma_1, \dots, \gamma_4$.

To obtain the energy bands for tight-binding model with nearest-neighbor (NN) hopping on the $\{8, 3\}$ lattice from HBT, the Bolza cell is equipped with twisted boundary conditions [9], defined by four phase factors, $e^{ik_1}, \dots, e^{ik_4}$, along the directions of the four generators: each bond crossing one

* corresponding author: tomas.bzdusek@psi.ch

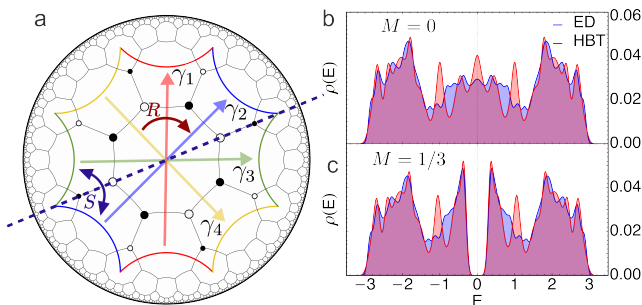


FIG. 1. **Nearest-neighbor model on the $\{8, 3\}$ lattice.** **a.** The lattice consists of octagons with coordination number three. The Bolza cell (multi-colored octagon), the fundamental tile of the hyperbolic Bravais lattice, contains six elementary octagons and 16 sites (black/white dots). The colored arrows labelled $\gamma_1, \dots, \gamma_4$ are the generators of the hyperbolic Bravais lattice. Rotation R (dark red) and reflection S (dark blue) are symmetries of the model. **b, c.** Bulk density of states $\rho(E)$ for the nearest-neighbor model on the $\{8, 3\}$ -lattice, extracted from hyperbolic band theory (HBT, red) vs. exact diagonalization (ED, blue) in the absence (**b**) vs. presence (**c**) of a sublattice potential M .

of the eight sides of the Bolza cell acquires a phase factor. This yields a 16×16 *hyperbolic Bloch Hamiltonian* $\mathcal{H}_{\text{Bloch}}(\mathbf{k})$, whose eigenvalues comprise 16 energy bands of the $\{8, 3\}$ lattice in 4D momentum space. We henceforth set the NN hopping parameter to unity.

The density of states (DoS) of tight-binding models, $\rho(E)$, can be obtained either (1) through exact diagonalization (ED) on finite hyperbolic graphs, or (2) via HBT by sampling \mathbf{k} over the 4D BZ. We refer to finite hyperbolic graphs with open boundary as *flakes*. To remove the contribution of boundary states, we define in ED calculations the *bulk-DoS* as the sum of local-DoS on the 16 sites in the innermost Bolza cell [44]. Whether the two just-defined DoS functions should match for large systems remains at present an open problem, since HBT only identifies eigenstates transforming in Abelian representations of the non-commutative translation group [45]. Nevertheless, the results for the NN model, compared in Fig. 1**b**, indicate an auspicious level of agreement, with the deviations partly attributable to residual boundary effects [46].

We next consider the inclusion of an on-site potential $\pm M$ with opposite sign on the two sublattices of the $\{8, 3\}$ lattice, marked with white/black in Fig. 1**a**. In the absence of a sublattice potential, the DoS is gapless at $E = 0$, whereas we observe a gap $\Delta E = 2M$ for $M \neq 0$. This feature is reproduced both with ED and HBT. In fact, for all tight-binding models studied in this work, whenever HBT predicts a gap in the DoS at certain energies, then a bulk gap is also found in this energy range with ED on flakes. Whether this behavior generalizes to all hyperbolic lattice models constitutes a formidable question for future investigations.

Topological band insulators.—We introduce the *hyperbolic Haldane model* on the $\{8, 3\}$ lattice by including complex-valued next-to-nearest-neighbor hopping terms, $t_2 e^{\pm i\Phi}$, to the tight-binding Hamiltonian of the previous section. The positive (negative) sign is chosen in the exponent for hopping

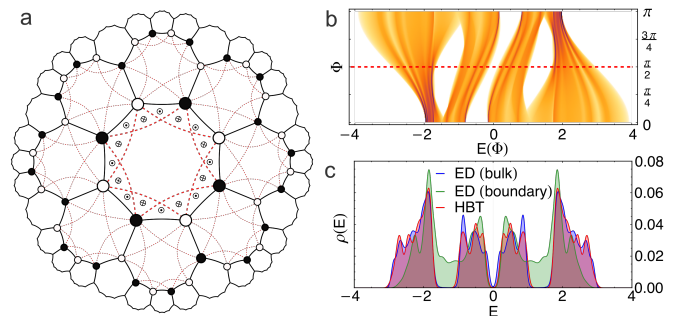


FIG. 2. **Hyperbolic Haldane model.** **a.** Schematic depiction of the model. Red dashed lines indicate next-to-nearest neighbor hopping with amplitude $t_2 e^{\pm i\Phi}$. The phases $\pm\Phi$ arise due to alternating magnetic fluxes (symbols \odot resp. \otimes in the innermost octagon) through the system. **b.** Density of states (DoS) for $t_2 = \frac{M}{2} = \frac{1}{6}$ computed from HBT, revealing three energy gaps. **c.** Bulk-DoS functions $\rho^{\text{HBT}}(E)$ and $\rho^{\text{ED}}_{\text{bulk}}(E)$ for $\Phi = \frac{\pi}{2}$ (red dashed line in **b**) computed using HBT (red) and ED (blue), and the boundary-DoS $\rho^{\text{ED}}_{\text{boundary}}$ (green).

in the clockwise (counter-clockwise) direction within an octagon. This model describes spinless fermions coupled orbitally to staggered magnetic fluxes, see Fig. 2**a**. The associated Bloch Hamiltonian $\mathcal{H}_{\text{H}}(\mathbf{k})$ with crystal momentum $\mathbf{k} = (k_1, k_2, k_3, k_4)$ is constructed using HBT [44]. The magnetic field breaks time-reversal symmetry, locating the model in Altland-Zirnbauer class A [28, 47]; we therefore anticipate that its topology is encoded by the Chern class [29, 48].

We investigate in Fig. 2**b** the model in terms of the DoS function $\rho^{\text{HBT}}(E; \Phi)$ as Φ is varied for $t_2 = M/2 = 1/6$. We identify extended gapped regions at filling fractions $f = \frac{5}{16}, \frac{8}{16}, \frac{11}{16}$, corresponding respectively to chemical potentials $\mu = -1.3, 0, 1.3$ at $\Phi = \pi/2$. (In contrast to the Euclidean case, non-vanishing $M \neq 0$ is necessary to open an energy gap at half-filling for the hyperbolic Haldane model [44].) In Fig. 2**c** we observe that the bulk gaps obtained from ED on flakes resp. from HBT again agree. Two of the three gaps are special in that they are filled by boundary states, as is inferred from ED by integrating the local-DoS over boundary sites [44]. Below, we reveal that these energy gaps are associated with non-trivial Chern topology and chiral edge states.

Next we introduce the *hyperbolic Kane-Mele (KM) model* of spin- $\frac{1}{2}$ fermions on the $\{8, 3\}$ lattice as a time-reversal-symmetric topological model in Altland-Zirnbauer class AII. The model can be interpreted as a “doubled” version of the Haldane model, graded with a spin degree of freedom, in the following sense [31, 49]: denoting the Hamiltonian of the Haldane model by \mathcal{H}_{H} , the Kane-Mele Hamiltonian for the spin-up (spin-down) fermions reads $\mathcal{H}_{\text{H}} (\mathcal{H}_{\text{H}}^*)$, and is supplied with spin-mixing Rashba term with amplitude λ_{R} . Since the hyperbolic curvature induces non-trivial holonomy of the spin along closed loops of the lattice, constructing a symmetry-compatible Rashba term is challenging. We therefore simplify the model here by assuming a non-constant curvature that is concentrated at the corners of the Bolza cell, while the curvature is flat everywhere else (for detailed construction see Supplementary Fig. S1 [44]). We call this simplified model

TABLE I. Values of topological invariants for the considered hyperbolic models, with the three energy gaps labelled by their filling fraction (f) and chemical potential (μ).

		Haldane				Kane-Mele			
f	μ	C_a	C_b	C_c	C_{RS}	ν_a	ν_b	ν_c	ν_{RS}
5/16	-1.3	-1	+1	-1	-0.986	1	1	1	-0.971
8/16	0	0	0	0	0	0	0	0	0
11/16	+1.3	-1	+1	-1	-0.986	1	1	1	-0.971

the *reduced hyperbolic KM model*.

The reduced KM model is expected to exhibit energy gaps at the same filling fractions as the Haldane model as long as λ_R is sufficiently small. This is verified by the plot of $\rho^{\text{HBT}}(E; \lambda_R)$ in Fig. 3a. The obtained data motivate us to fix $\lambda_R = -1/6$, in which case all three gaps are still present. The comparison of the resulting $\rho^{\text{HBT}}(E)$ and $\rho_{\text{bulk}}^{\text{ED}}(E)$ is shown in Fig. 3b. The same panel also displays the corresponding $\rho_{\text{boundary}}^{\text{ED}}(E)$, which reveals filling of the two outer energy gaps by edge states, portending a non-trivial Kane-Mele topology.

Topological invariants.—We compute topological invariants in momentum and position space for the band gaps of both constructed models. In \mathbf{k} -space, we compute the first Chern numbers of the Haldane model from the Bloch Hamiltonian $\mathcal{H}_H(\mathbf{k})$ in the six planes spanned by pairs (k_i, k_j) of momentum components, $i, j = 1, \dots, 4$. The model exhibits $(\pi/2)$ -rotation symmetry R around the center of the Bolza cell [dark red arrow in Fig. 1(a)], which transforms the group generators as $(\gamma_1, \gamma_2, \gamma_3, \gamma_4) \mapsto (\gamma_3, \gamma_4, \gamma_1^{-1}, \gamma_2^{-1})$; therefore, the Hamiltonians $\mathcal{H}_H(k_1, k_2, k_3, k_4)$ and $\mathcal{H}_H(k_3, k_4, -k_1, -k_2)$ are related by a unitary transformation. Consequently, one can relate Chern numbers $C_{12} = C_{34} =: C_a$ and $C_{14} = C_{23} =: C_c$. In addition, while reflection S [dashed blue line in Fig. 1(a)] flips the magnetic fluxes $\pm\Phi$, its composition with time-reversal constitutes an antiunitary symmetry of the Haldane model, transforming $(k_1, k_2, k_3, k_4) \mapsto (-k_4, -k_3, -k_2, -k_1)$ and relating $C_{13} = C_{24} =: C_b$. We compute $C_{a,b,c}$ using Wilson loops [50, 51], and find that energy gaps at $f = \frac{5}{16}, \frac{11}{16}$ have non-trivial Chern number ± 1 in all planes, while the gap at $f = \frac{8}{16}$ does not exhibit Chern topology, see Table I. Similarly, after utilizing the R and S symmetry of $\mathcal{H}_{KM}(\mathbf{k})$, we identify three independent \mathbb{Z}_2 -topological invariants ν_{ij} , namely $\nu_a := \nu_{12} = \nu_{34}$, $\nu_b := \nu_{13} = \nu_{24}$, and $\nu_c := \nu_{14} = \nu_{23}$. We find that $\nu_{a,b,c}$ are all non-trivial for the two outer band gaps, while they are trivial for the inner gap, see Table I. [We discuss in the Supplementary Material [44] that if $M = 0$ then an additional $(\pi/4)$ -rotation symmetry further implies $C_a = C_c$ and $\nu_a = \nu_c$].

We also computed higher-dimensional topological invariants for $\mathcal{H}_H(\mathbf{k})$ and $\mathcal{H}_{KM}(\mathbf{k})$, namely the \mathbb{Z}_2 -valued Fu-Kane-Mele [52] invariant on 3D subspaces (for KM) and the second Chern number [48, 53] in 4D BZ (for both). These, however, are all trivial. Nevertheless, hyperbolic toy-models with non-vanishing values of such topological invariants could be constructed through reverse engineering: starting from a 4D Euclidean Bloch-Hamiltonian, $\mathcal{H}_{\text{Euc}}(\mathbf{k})$, which features such topological invariants, one constructs a hyperbolic tight-

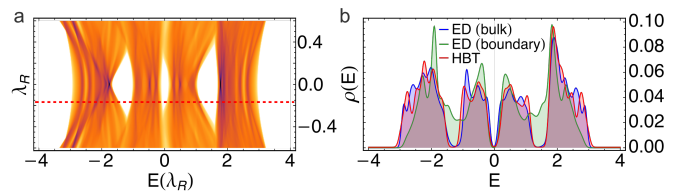


FIG. 3. **Hyperbolic Kane-Mele model.** **a.** Density of states (DoS) for $t_2 = \frac{M}{2} = \frac{1}{6}$ computed from HBT, which reveals three energy gaps at small Rashba coupling λ_R . **b.** Bulk-DoS functions for $\lambda_R = -\frac{1}{6}$ (red dashed line in **a**) computed using HBT (red) and ED (blue), and the boundary-DoS function (green).

binding model where each component k_i of \mathbf{k} is replaced by a generator γ_i of the hyperbolic Bravais lattice. We leave this promising route for designing topological hyperbolic Hamiltonians for future research.

We complement the momentum-space discussion of the band topology of the two models with real-space topological markers [38–42]. Importantly, these computations include states transforming in *all* representations of the non-commutative translation group, hence going beyond HBT. For the Haldane model, we compute the *real-space Chern number* C_{RS} as introduced in Ref. 39 (detailed in Supplementary Material [44]). This algorithm does not warrant quantized results, but we confirm that integers are approached as the summation regions are enlarged. Our position-space analysis confirms that the energy gaps at $\mu = \pm 1.3$ are topological, while the one at $\mu = 0$ is trivial, see Table I. We observe $C_{RS} = C_a = -C_b = C_c$ for all phases with gapped bulk. Recall here that for 2D Euclidean lattices we have $C_{RS} = C_{12}$ [38, 39], whereas no exact relation is currently known for hyperbolic lattices.

We further adapt the techniques of Refs. 39–42 to compute the *real-space spin Chern number* $\nu_{RS} \in \mathbb{Z}$ of the reduced KM model for each bulk gap. This invariant is integer-valued as long as spin-mixing terms in the Hamiltonian are sufficiently weak, and for Euclidean lattice models it obeys $\nu_{RS} = \nu_{12} \pmod{2}$ [41, 42]. We observe that the extracted \mathbb{Z}_2 -invariants obey $\nu_{RS} = \nu_a = \nu_b = \nu_c$ for all cases analyzed. Whether there exists a simple *universal* relation between the parities of $\nu_{a,b,c,RS}$ constitutes another open question.

Bulk-boundary correspondence.—We finally investigate whether the non-trivial band topology identified in the bulk for both models is reflected in topological edge states on the boundary. For this, we (i) extract the edge-state dispersion, (ii) showcase the propagation of an edge-localized wave packet around the flake boundary, and (iii) investigate their robustness against disorder.

(i) When computing for a circular flake the edge-state dispersion (E) against angular momentum (ℓ), note that the latter is only defined modulo 4 due to the fourfold symmetry R . To obtain $E(\ell)$ for *unbounded* $\ell \in \mathbb{Z}$, we decompose the lattice eigenstates $|\phi_j\rangle$ into eigenmodes $|\psi_{n,\ell}\rangle$ of the Laplace-Beltrami operator defined in the continuum [6, 13] and select the number ℓ with the largest contribution (for details see Supplementary Material [44]). We plot $E(\ell)$ for the edge states in

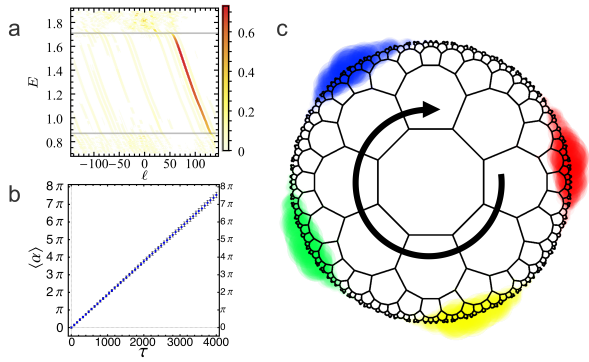


FIG. 4. **Topological edge states.** **a.** Edge-dispersion E as a function of angular momentum ℓ for chiral edge states in the upper energy gap of the hyperbolic Haldane model. **b.** Propagation of a Gaussian wave packet along the flake boundary; $\langle \alpha \rangle$ is the angular displacement in time τ , and error bars indicate the width of the wave packet. **c.** Snapshots of the wave packet at $\tau = 0, 240, 480, 720$ (colored respectively red/yellow/green/blue). The area of a disk centered at a given site encodes the probability to find the particle at that site.

the hyperbolic Haldane model for the energy gap at $\mu = 1.3$ in Fig. 4a. We observe a single dispersive branch for positive ℓ only, implying chiral edge state at the flake boundary, in agreement with $|C_{RS}| = 1$. An analogous analysis for the reduced Kane-Mele model at the same filling reveals a pair of counter-propagating *helical* branches, compatible with $|v_{RS}| = 1$ (see Supplementary Fig. S7 [44]).

(ii) To study the propagation of a *wave packet* along the edge, we construct a boundary-localized Gaussian state with energy near μ and with energy width σ [44]. We plot in Fig. 4b,c the time-evolution of a wave packet initialized with parameters $(\mu, \sigma) = (1.3, 0.025)$ in the hyperbolic Haldane model. We find the center of the packet smoothly propagates along the boundary in time. The angular group velocity of the wave packet extracted from the time-evolution matches the edge-dispersion from (i) via $\omega_{\text{group}} = dE/d\ell$. We similarly analyzed the edge-state propagation for the reduced KM model [44] and confirmed their anticipated helical character.

(iii) To quantify the robustness of the edge states against Anderson localization when subject to disorder, we show that they retain a small *inverse participation ratio* (IPR). Here $0 < \text{IPR} \leq 1$ is defined such that an eigenstate $|\phi_j\rangle$ characterized by value IPR_j has most support over approximately $1/\text{IPR}_j$ sites [44]. For the reduced KM model, we add random spin-mixing terms that either preserve (TRS) or break (TRB) time-reversal symmetry of the model. These can be interpreted as *random Rashba terms* resp. *random magnetic fields*, with an amplitude $W \in [-W_{\text{max}}, W_{\text{max}}]$ drawn from a uniform distribution. The results in Fig. 5 indicate that disorder with TRB leads to localization of the edge states, whereas increasing W_{max} in the presence of TRS does not change their IPR values significantly, as expected for topological edge states. We similarly verified for the hyperbolic Haldane model that inclusion of random on-site potential drawn from a uniform distribution $W \in [-W_{\text{max}}, W_{\text{max}}]$ has little effect on the IPR of the edge states. In addition, we confirmed that the chiral prop-

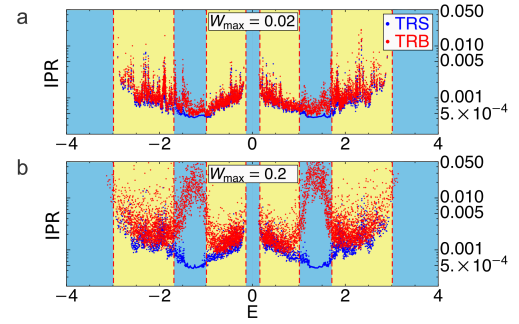


FIG. 5. **Robustness against Anderson localization.** For the reduced hyperbolic KM model, we consider inclusion of random spin-mixing terms that preserve (TRS, blue) or break (TRB, red) time-reversal symmetry. A dot with coordinates (E_j, IPR_j) represents the energy and the inverse participation ratio of an eigenstate $|\phi_j\rangle$ in the flake geometry. The random terms are drawn from a uniform distribution with $W_{\text{max}} = 0.02$ (a) and $W_{\text{max}} = 0.2$ (b). The blue (yellow) backgrounds indicate energy ranges corresponding to bulk gap (bulk band) in the absence of disorder.

agation of the edge states without back-scattering is preserved under the addition of the random terms (see Supplementary Fig. S4 [44]). This provides further evidence of the non-trivial topology of the constructed model.

Outlook.—Our work constitutes an essential step towards designing topological hyperbolic Hamiltonians and exploring the interplay of geometry and topology in such systems. It is natural to wonder if similar constructions of topological insulators generalize to other hyperbolic $\{p, q\}$ lattices. Indeed, the Haldane model on the $\{6, 4\}$ lattice has very recently been implemented as an electric-circuit network by Ref. 25, while another model of Chern insulator on the $\{8, 3\}$ lattice, although lacking translation symmetry, has been considered by Ref. 26. However, these works did not apply HBT to characterize the models, thus lacking the momentum-space language.

A key difference between hyperbolic and Euclidean lattices is the extensive scaling of the boundary in the hyperbolic case, implying a finite fraction of boundary sites *irrespective* of the system size [13, 22]. Consequently, a *macroscopic fraction of all states* contributes to topological edge modes, in stark contrast to Euclidean topological models. It will be intriguing to investigate features of non-Hermitian topology in this context, as the non-Hermitian skin effect likewise affects a macroscopic fraction of the spectrum [54–59]. The extensive hyperbolic boundary is also anticipated to give access to novel one-dimensional many-body models affected by the bulk design through the bulk-boundary correspondence.

Code and data availability.—The Wolfram Language code and the generated data used to arrive at the conclusions presented in this work are publicly available in the following data repository: <https://doi.org/10.5281/zenodo.6380568> [60]. The manuscript is based on the master’s thesis of one of the authors [49].

Acknowledgments.—We would like to express our thanks to M. Brzezińska, A. Chen, B. Lapierre, J. Maciejko, A. Stegmaier, T. Tummuru, and L. K. Upreti for helpful discussions. P. M. L. and T. B. were supported by the

Ambizione grant No. 185806 by the Swiss National Science Foundation. I. B. acknowledges support from the University of Alberta startup fund UOFAB Startup Boettcher and the Natural Sciences and Engineering Research Council of Canada (NSERC) Discovery Grants RGPIN-2021-02534 and DGECR2021-00043. R. T. acknowledges funding by the Deutsche Forschungsgemeinschaft (DFG, German Re-



search Foundation) through Project-ID 258499086 - SFB 1170, and through the Würzburg-Dresden Cluster of Excellence on Complexity and Topology in Quantum Matter – *ct.qmat* Project-ID 39085490 - EXC 2147. T. N. acknowledges support from the European Research Council (ERC) under the European Union’s Horizon 2020 research and innovation program (ERC-StG-Neupert-757867-PARATOP).

-
- [1] Barry Bradlyn, L. Elcoro, Jennifer Cano, M. G. Vergniory, Zhijun Wang, C. Felser, M. I. Aroyo, and B. Andrei Bernevig, “Topological quantum chemistry,” *Nature* **547**, 298–305 (2017).
- [2] Hoi Chun Po, Ashvin Vishwanath, and Haruki Watanabe, “Symmetry-based indicators of band topology in the 230 space groups,” *Nat. Commun.* **8**, 50 (2017).
- [3] Maia G. Vergniory, Benjamin J. Wieder, Luis Elcoro, Stuart S. P. Parkin, Claudia Felser, B. Andrei Bernevig, and Nicolas Regnault, “All topological bands of all nonmagnetic stoichiometric materials,” *Science* **376**, abg9094 (2022).
- [4] Eva Y. Andrei, Dmitri K. Efetov, Pablo Jarillo-Herrero, Allan H. MacDonald, Kin Fai Mak, T. Senthil, Emanuel Tutuc, Ali Yazdani, and Andrea F. Young, “The marvels of moiré materials,” *Nat. Rev. Mater.* **6**, 201–206 (2021).
- [5] Alicia J. Kollár, Mattias Fitzpatrick, and Andrew A. Houck, “Hyperbolic lattices in circuit quantum electrodynamics,” *Nature* **571**, 45 (2019).
- [6] Patrick M. Lenggenhager, Alexander Stegmaier, Lavi K. Upreti, Tobias Hofmann, Tobias Helbig, Achim Vollhardt, Martin Greiter, Ching Hua Lee, Stefan Imhof, Hauke Brand, Tobias Kießling, Igor Boettcher, Titus Neupert, Ronny Thomale, and Tomáš Bzdušek, “Simulating hyperbolic space on a circuit board,” *Nat. Commun.* **13**, 4373 (2022).
- [7] W. Magnus, *Noneuclidean tessellations and their groups* (Academic Press, New York, 1974).
- [8] H. S. M. Coxeter and W. O. J. Moser, *Generators and Relations for Discrete Groups* (Springer Berlin Heidelberg, Berlin, Heidelberg, 1980).
- [9] Joseph Maciejko and Steven Rayan, “Hyperbolic band theory,” *Sci. Adv.* **7**, eabe9170 (2021).
- [10] Sunkyu Yu, Xianji Piao, and Namkyoo Park, “Topological Hyperbolic Lattices,” *Phys. Rev. Lett.* **125**, 053901 (2020).
- [11] Kazuki Ikeda, Shoto Aoki, and Yoshiyuki Matsuki, “Hyperbolic band theory under magnetic field and Dirac cones on a higher genus surface,” *J. Phys. Condens. Matter* **33**, 485602 (2021).
- [12] Alexander Stegmaier, Lavi K. Upreti, Ronny Thomale, and Igor Boettcher, “Universality of hofstadter butterflies on hyperbolic lattices,” *Phys. Rev. Lett.* **128**, 166402 (2022).
- [13] Igor Boettcher, Przemyslaw Bienias, Ron Belyansky, Alicia J. Kollár, and Alexey V. Gorshkov, “Quantum simulation of hyperbolic space with circuit quantum electrodynamics: From graphs to geometry,” *Phys. Rev. A* **102**, 032208 (2020).
- [14] Joseph Maciejko and Steven Rayan, “Automorphic Bloch theorems for hyperbolic lattices,” *Proc. Natl. Acad. Sci. U.S.A.* **119**, e2116869119 (2022).
- [15] Xingchuan Zhu, Jiaojiao Guo, Nikolas P. Breuckmann, Huaiming Guo, and Shipping Feng, “Quantum phase transitions of interacting bosons on hyperbolic lattices,” *J. Phys. Condens. Matter* **33**, 335602 (2021).
- [16] Nikolas P. Breuckmann and Barbara M. Terhal, “Constructions and Noise Threshold of Hyperbolic Surface Codes,” *IEEE Trans. Inf. Theory* **62**, 3731–3744 (2016).
- [17] Igor Boettcher, Alexey V. Gorshkov, Alicia J. Kollár, Joseph Maciejko, Steven Rayan, and Ronny Thomale, “Crystallography of hyperbolic lattices,” *Phys. Rev. B* **105**, 125118 (2022).
- [18] Przemyslaw Bienias, Igor Boettcher, Ron Belyansky, Alicia J. Kollár, and Alexey V. Gorshkov, “Circuit quantum electrodynamics in hyperbolic space: From photon bound states to frustrated spin models,” *Phys. Rev. Lett.* **128**, 013601 (2022).
- [19] Adil Attar and Igor Boettcher, “Selberg trace formula in hyperbolic band theory,” *Phys. Rev. E* **106**, 034114 (2022).
- [20] Massimo Ruzzene, Emil Prodan, and Camelia Prodan, “Dynamics of elastic hyperbolic lattices,” *Extreme Mech. Lett.* **49**, 101491 (2021).
- [21] Alicia J. Kollár, Mattias Fitzpatrick, Peter Sarnak Sarnak, and Houck. Andrew A., “Line-Graph Lattices: Euclidean and Non-Euclidean Flat Bands, and Implementations in Circuit Quantum Electrodynamics,” *Commun. Math. Phys.* **376**, 1909–1956 (2019).
- [22] Alberto Saa, Eduardo Miranda, and Francisco Rouxinol, “Higher-dimensional Euclidean and non-Euclidean structures in planar circuit quantum electrodynamics,” (2021), [arXiv:2108.08854 \[quant-ph\]](https://arxiv.org/abs/2108.08854).
- [23] Tomáš Bzdušek and Joseph Maciejko, “Flat bands and bandtouching from real-space topology in hyperbolic lattices,” *Phys. Rev. B* **106**, 155146 (2022).
- [24] Rémy Mosseri, Roger Vogeler, and Julien Vidal, “Aharonov-Bohm cages, flat bands, and gap labeling in hyperbolic tilings,” *Phys. Rev. B* **106**, 155120 (2022).
- [25] Weixuan Zhang, Hao Yuan, Na Sun, Houjun Sun, and Xiangdong Zhang, “Observation of novel topological states in hyperbolic lattices,” *Nat. Commun* **13**, 2937 (2022).
- [26] Zheng-Rong Liu, Chun-Bo Hua, Tan Peng, and Bin Zhou, “Chern insulator in a hyperbolic lattice,” *Phys. Rev. B* **105**, 245301 (2022).
- [27] Svetlana Katok, *Fuchsian groups* (University of Chicago press, Chicago, 1992).
- [28] Alexei Kitaev, “Periodic table for topological insulators and superconductors,” *AIP Conf. Proc.* **1134**, 22 (2009).
- [29] Shinsei Ryu, Andreas P. Schnyder, Akira Furusaki, and Andreas W. W. Ludwig, “Topological insulators and superconductors: tenfold way and dimensional hierarchy,” *New J. Phys.* **12**, 065010 (2010).
- [30] F. D. M. Haldane, “Model for a Quantum Hall Effect without Landau Levels: Condensed-Matter Realization of the “Parity Anomaly”,” *Phys. Rev. Lett.* **61**, 2015–2018 (1988).
- [31] C. L. Kane and E. J. Mele, “ Z_2 Topological Order and the Quantum Spin Hall Effect,” *Phys. Rev. Lett.* **95**, 146802 (2005).
- [32] Alexander B. Khanikaev, S. Hossein Mousavi, Wang-Kong Tse, Mehdi Kargarian, Allan H. MacDonald, and Gennady Shvets, “Photonic topological insulators,” *Nat. Mater.* **12**, 233–239 (2013).

- [33] Gregor Jotzu, Michael Messer, Rémi Desbuquois, Martin Lebrat, Thomas Uehlinger, Daniel Greif, and Tilman Esslinger, “Experimental realization of the topological Haldane model with ultracold fermions,” *Nature* **515**, 237–240 (2014).
- [34] Yujiang Ding, Yugui Peng, Yifan Zhu, Xudong Fan, Jing Yang, Bin Liang, Xuefeng Zhu, Xiangang Wan, and Jianchun Cheng, “Experimental Demonstration of Acoustic Chern Insulators,” *Phys. Rev. Lett.* **122**, 014302 (2019).
- [35] Stefan Imhof, Christian Berger, Florian Bayer, Johannes Brehm, Laurens W. Molenkamp, Tobias Kiessling, Frank Schindler, Ching Hua Lee, Martin Greiter, Titus Neupert, and Ronny Thomale, “Topoelectrical-circuit realization of topological corner modes,” *Nat. Phys.* **14**, 925 (2018).
- [36] Ching Hua Lee, Stefan Imhof, Christian Berger, Florian Bayer, Johannes Brehm, Laurens W. Molenkamp, Tobias Kiessling, and Ronny Thomale, “Topoelectrical Circuits,” *Commun. Phys.* **1**, 39 (2018).
- [37] Tobias Hofmann, Tobias Helbig, Ching Hua Lee, Martin Greiter, and Ronny Thomale, “Chiral Voltage Propagation and Calibration in a Topoelectrical Chern Circuit,” *Phys. Rev. Lett.* **122**, 247702 (2019).
- [38] J. Bellissard, A. van Elst, and H. Schulz-Baldes, “The noncommutative geometry of the quantum Hall effect,” *J. Math. Phys.* **35**, 5373–5451 (1994).
- [39] Alexei Kitaev, “Anyons in an exactly solved model and beyond,” *Ann. Phys.* **321**, 2–111 (2006).
- [40] Raffaello Bianco and Raffaele Resta, “Mapping topological order in coordinate space,” *Phys. Rev. B* **84**, 241106(R) (2011).
- [41] Emil Prodan, “Disordered topological insulators: a noncommutative geometry perspective,” *J. Phys. A Math. Theor.* **44**, 113001 (2011).
- [42] Huaqing Huang and Feng Liu, “Theory of spin Bott index for quantum spin Hall states in nonperiodic systems,” *Phys. Rev. B* **98**, 125130 (2018).
- [43] M. E. Kazaryan, S. K. Lando, and V. V. Prasolov, *Algebraic Curves: Towards Moduli Spaces*, Moscow Lectures, Vol. 2 (Springer, Cham, Switzerland, 2019).
- [44] The Supplemental Material contains supporting data and detailed information about the methods.
- [45] Nan Cheng, Francesco Serafin, James McInerney, Zeb Rocklin, Kai Sun, and Xiaoming Mao, “Band Theory and Boundary Modes of High-Dimensional Representations of Infinite Hyperbolic Lattices,” *Phys. Rev. Lett.* **129**, 088002 (2022).
- [46] Anffany Chen, Hauke Brand, Tobias Helbig, Tobias Hofmann, Stefan Imhof, Alexander Fritzsche, Tobias Kießling, Alexander Stegmaier, Lavi K. Upreti, Titus Neupert, Tomáš Bzdušek, Martin Greiter, Ronny Thomale, and Igor Boettcher, “Hyperbolic matter in electrical circuits with tunable complex phases,” (2022), [arXiv:2205.05106](https://arxiv.org/abs/2205.05106).
- [47] Alexander Altland and Martin R. Zirnbauer, “Nonstandard symmetry classes in mesoscopic normal-superconducting hybrid structures,” *Phys. Rev. B* **55**, 1142–1161 (1997).
- [48] Mikio Nakahara, *Geometry, topology and physics*, Graduate student series in physics (Hilger, Bristol, 1990).
- [49] David M. Urwyler, *Hyperbolic Topological Insulator*, Master’s thesis, University of Zürich, Switzerland (2021); David M. Urwyler, Patrick M. Lenggenhager, Titus Neupert, and Tomáš Bzdušek, “Topological hyperbolic band insulators,” (2022), APS March Meeting 2022, Session N66.
- [50] Alexey A. Soluyanov and David Vanderbilt, “Computing topological invariants without inversion symmetry,” *Phys. Rev. B* **83**, 235401 (2011).
- [51] Dominik Gresch, Gabriel Autès, Oleg V. Yazyev, Matthias Troyer, David Vanderbilt, B. Andrei Bernevig, and Alexey A. Soluyanov, “Z2Pack: Numerical implementation of hybrid Wannier centers for identifying topological materials,” *Phys. Rev. B* **95**, 075146 (2017).
- [52] Liang Fu, C. L. Kane, and E. J. Mele, “Topological Insulators in Three Dimensions,” *Phys. Rev. Lett.* **98**, 106803 (2007).
- [53] Shou-Cheng Zhang and Jiangping Hu, “A Four-Dimensional Generalization of the Quantum Hall Effect,” *Science* **294**, 823–828 (2001).
- [54] Dan S. Borgnia, Alex Jura Kruchkov, and Robert-Jan Slager, “Non-hermitian boundary modes and topology,” *Phys. Rev. Lett.* **124**, 056802 (2020).
- [55] Nobuyuki Okuma, Kohei Kawabata, Ken Shiozaki, and Masatoshi Sato, “Topological Origin of Non-Hermitian Skin Effects,” *Phys. Rev. Lett.* **124**, 086801 (2020).
- [56] Sebastian Weidemann, Mark Kremer, Tobias Helbig, Tobias Hofmann, Alexander Stegmaier, Martin Greiter, Ronny Thomale, and Alexander Szameit, “Topological funneling of light,” *Science* **368**, 311–314 (2020).
- [57] Tobias Hofmann, Tobias Helbig, Frank Schindler, Nora Salgo, Marta Brzezińska, Martin Greiter, Tobias Kiessling, David Wolf, Achim Vollhardt, Anton Kabaši, Ching Hua Lee, Ante Bilušić, Ronny Thomale, and Titus Neupert, “Reciprocal skin effect and its realization in a topoelectrical circuit,” *Phys. Rev. Research* **2**, 023265 (2020).
- [58] T. Helbig, T. Hofmann, S. Imhof, M. Abdelghany, T. Kiessling, L. W. Molenkamp, C. H. Lee, A. Szameit, M. Greiter, and R. Thomale, “Generalized bulk–boundary correspondence in non-hermitian topoelectrical circuits,” *Nat. Phys.* **16**, 747–750 (2020).
- [59] Chenwei Lv, Ren Zhang, Zhengzheng Zhai, and Qi Zhou, “Curving the space by non-Hermiticity,” *Nat. Commun.* **13**, 2184 (2022).
- [60] David M. Urwyler, Patrick M. Lenggenhager, Igor Boettcher, Ronny Thomale, Titus Neupert, and Tomáš Bzdušek, “Data and code for: Hyperbolic topological band insulators,” (2022), DOI: <https://doi.org/10.5281/zenodo.6380568>.

Supplementary Material to:

Hyperbolic Topological Band Insulators

David M. Urwyler,¹ Patrick M. Lenggenhager ^{1,2,3} Igor Boettcher ^{4,5}

Ronny Thomale ⁶ Titus Neupert ¹ and Tomáš Bzdušek ^{2,1,*}

¹*Department of Physics, University of Zurich, Winterthurerstrasse 190, 8057 Zurich, Switzerland*

²*Condensed Matter Theory Group, Paul Scherrer Institute, 5232 Villigen PSI, Switzerland*

³*Institute for Theoretical Physics, ETH Zurich, 8093 Zurich, Switzerland*

⁴*Department of Physics, University of Alberta, Edmonton, Alberta T6G 2E1, Canada*

⁵*Theoretical Physics Institute, University of Alberta, Edmonton, Alberta T6G 2E1, Canada*

⁶*Institut für Theoretische Physik und Astrophysik, Universität Würzburg, 97074 Würzburg, Germany*

(Dated: January 10, 2023)

Contents

S1. Geometry of the hyperbolic plane.	2
S2. Geometry of $\{p, q\}$ tessellations.	3
S3. Reduced Kane-Mele model.	4
S4. Hyperbolic Bloch Hamiltonian.	6
S5. Flake Hamiltonian in position space.	7
S6. Considered system sizes in the flake geometry.	8
S7. Bulk density of states and integrated boundary density of states for the flake Hamiltonian.	9
S8. Real-space invariants.	10
S9. Gaussian projector operator.	11
S10. Models of disorder.	12
S11. Hyperbolic Bloch Hamiltonians of the studied models	13
S12. Wilson-loop extraction of topological band invariants	15
S13. Extraction of the edge mode dispersion	17
S14. Group velocity of the chiral edge states in hyperbolic Haldane model	22
S15. Phase diagram of the hyperbolic Haldane Bloch Hamiltonian at half-filling and $\Phi = \pi/2$	23

* corresponding author: tomas.bzdusek@psi.ch

Supplementary Note S1: Geometry of the hyperbolic plane.

We adopt the Poincaré-disk representation of the hyperbolic plane, i.e., as the unit disk in the complex plane, $\mathbb{D} = \{z \in \mathbb{C} \mid |z| < 1\}$, with the hyperbolic metric given by

$$ds^2 = (2\kappa)^2 \frac{dz d\bar{z}}{(1 - z\bar{z})^2}, \quad (\text{S1})$$

where κ is a unit of length and the bar in \bar{z} indicates complex conjugation. With this choice, the Gaussian curvature equals $K = -\kappa^2$. In our work, we fix $\kappa = 1/2$ (leading to curvature $K = -4$). With this convention,

$$d(z_1, z_2) = \frac{1}{2} \operatorname{arcosh} \left[1 + \frac{2|z_1 - z_2|^2}{(1 - |z_1|^2)(1 - |z_2|^2)} \right] \quad (\text{S2})$$

determines the geodesic distance for a pair of points $z_{1,2} \in \mathbb{D}$ [17].

We briefly investigate geometric aspects of a disk with radius $0 < R < 1$ in the complex plane, labelled \mathbb{D}_R . Its surface area is computed as

$$S(R) = \int_0^{2\pi} d\phi \int_0^R dr \frac{r}{(1 - r^2)^2} = \frac{\pi R^2}{1 - R^2}. \quad (\text{S3})$$

The hyperbolic distance from the center to the boundary of the disk is

$$d(0, R) = \int_0^R \frac{dr}{(1 - r^2)} = \frac{1}{2} \operatorname{arcosh} \left(\frac{1 + R^2}{1 - R^2} \right) = \operatorname{artanh} R, \quad (\text{S4})$$

and its perimeter is

$$p(R) = \int_0^{2\pi} d\phi \frac{R}{(1 - R^2)} = \frac{2\pi R}{1 - R^2}. \quad (\text{S5})$$

It is easily verified that $p(R)/d(0, R) > 2\pi$ (for perimeter) and $S(R)/d^2(0, R) > \pi$ (for surface area), as expected for a negatively curved space.

Supplementary Note S2: Geometry of $\{p, q\}$ tessellations.

We determine the distance $d_1^{(p,q)}$ of nearest-neighbor vertices of the $\{p, q\}$ lattice. For that purpose, we consider a triangle ABC where: A is the center of a regular p -sided polygon (a ‘ p -gon’, for short), B is one of the p -gon’s vertices, and C is a point that lies on the boundary of the p -gon at the middle of an edge connecting to B . Note that the hyperbolic length of the triangle side $|BC| = d_1^{(p,q)}/2$. The internal angles of triangle ABC at vertices A , B , and C are identified as $\alpha = \pi/p$, $\beta = \pi/q$, and $\gamma = \pi/2$, respectively. According to the hyperbolic law of cosines [27],

$$\cosh\left(\frac{|BC|}{\kappa}\right) = \frac{\cos \alpha + \cos \beta \cos \gamma}{\sin \beta \sin \gamma} = \frac{\cos \frac{\pi}{p}}{\sin \frac{\pi}{q}}, \quad (\text{S6})$$

which implies $d_1^{(8,3)} = \text{arcosh}\left(\cos \frac{\pi}{8} / \sin \frac{\pi}{3}\right) \approx 0.36352$ for our choice $\kappa = 1/2$. Next, the distance $|AB| = r^{(p,q)}$ from the center of the p -gon to its vertex is also determined from the law of cosines,

$$\cosh\left(\frac{|AB|}{\kappa}\right) = \frac{\cos \gamma + \cos \alpha \cos \beta}{\sin \alpha \sin \beta} = \frac{1}{\tan \frac{\pi}{p} \tan \frac{\pi}{q}}, \quad (\text{S7})$$

leading to $r^{(8,3)} = \text{arcosh}\left[1 / \left(\tan \frac{\pi}{8} \tan \frac{\pi}{3}\right)\right] / 2 \approx 0.430353$.

If the center of the p -gon is placed at the center of the Poincaré disk ($z = 0$), then Eq. (S4) governs the complex coordinates of the p -gon vertices, $|z_B^{(p,q)}| = \tanh(r^{(p,q)})$, leading to $|z_B^{(8,3)}| \approx 0.405616$. The information obtained thus far is sufficient to find the complex coordinates $\{z_{(\emptyset, a)}\}_{a=1}^{n_{\text{cell}}}$ (where $n_{\text{cell}} = 16$) of all sites of the $\{8, 3\}$ lattice which reside inside the Bolza cell centered at $z = 0$ (listed in Supplementary Table S1). For later purposes, we use Eq. (S2) to also determine the distance of next-nearest-neighbor sites as

$$d_2^{(p,q)} = d\left(|z_B^{(p,q)}|e^{2\pi i/p}, |z_B^{(p,q)}|e^{-2\pi i/p}\right), \quad (\text{S8})$$

which leads to $d_2^{(8,3)} = \text{arcosh}\left(1 + \frac{2\sqrt{2}}{3}\right) / 2 \approx 0.641645$.

site label a	1	2	3	4
coordinate $z_{(\emptyset, a)}$	$0.374741 + 0.155223 i$	$0.155223 + 0.374741 i$	$-0.155223 + 0.374741 i$	$-0.374741 + 0.155223 i$
site label a	5	6	7	8
coordinate $z_{(\emptyset, a)}$	$-0.374741 - 0.155223 i$	$-0.155223 - 0.374741 i$	$0.155223 - 0.374741 i$	$0.374741 - 0.155223 i$
site label a	9	10	11	12
coordinate $z_{(\emptyset, a)}$	$0.610313 + 0.252800 i$	$0.252800 + 0.610313 i$	$-0.252800 + 0.610313 i$	$-0.610313 + 0.252800 i$
site label a	13	14	15	16
coordinate $z_{(\emptyset, a)}$	$-0.610313 - 0.252800 i$	$-0.252800 - 0.610313 i$	$0.252800 - 0.610313 i$	$0.610313 - 0.252800 i$

Supplementary Table S1. **Coordinates of the sites in the Bolza cell.** The table lists the complex coordinates of the 16 sites of the $\{8, 3\}$ lattice which belong to the innermost Bolza cell (centered at $z = 0$), represented inside the Poincaré disk with radius 1. For derivation of these values, and for the meaning of the subscript “ (\emptyset, a) ”, see Methods.

The Gauss-Bonnet theorem [48] relates surface area S^P of a geodesic p -sided polygon P in space of constant curvature K to its internal angles $\{\alpha_j\}_{j=1}^p$,

$$\sum_{j=1}^p (\pi - \alpha_j) = 2\pi - KS^P. \quad (\text{S9})$$

The elementary cell of the $\{p, q\}$ lattice is a regular geodesic p -gon with all internal angles of size $\alpha = 2\pi/q$. It follows from Eq. (S9) that the surface area of the elementary p -gon is

$$S^{(p,q)} = \pi \frac{(p-2)(q-2) - 4}{4q}. \quad (\text{S10})$$

We obtain $S^{(8,3)} = \pi/6$, while the area of the Bolza cell (p -gon of $\{8, 8\}$ lattice) is six times larger, $S^{\text{Bolza}} = \pi$. The ratio

$$\tilde{N}_{\text{UC}}(R) = \frac{S(R)}{S^{\text{Bolza}}} = \frac{R^2}{1 - R^2} \quad (\text{S11})$$

gives an approximate number of Bolza cells that fit into a disk with radius R in the complex plane.

Supplementary Note S3: Reduced Kane-Mele model.

To avoid complications that arise from non-trivial spin holonomy in curved spaces, we construct the *reduced* Kane-Mele (rhKM) model through the following simplification [cf. Supplementary Fig. S1]: instead of taking the negative curvature to be constant inside the Bolza cell, we consider a continuous deformation where all the curvature becomes concentrated at the corners of the cell (cyan dots in Supplementary Fig. S1) while the manifold becomes flat everywhere else. Then, the Bolza cell essentially becomes a Euclidean regular octagon (black outline in Supplementary Fig. S1). [Note that the adjacent Bolza cells (dashed frames in Supplementary Fig. S1) seemingly overlap one another, but this is consistent with the -4π quantum of curvature at the vertex.] Then there exists a unique arrangement of the 16 sites of the $\{8, 3\}$ lattice (blue frame in Supplementary Fig. S1) within the octagon such that (1) all pairs of NN sites have the same distance, and (2) the eightfold rotation and mirror symmetries of the octagon are preserved.

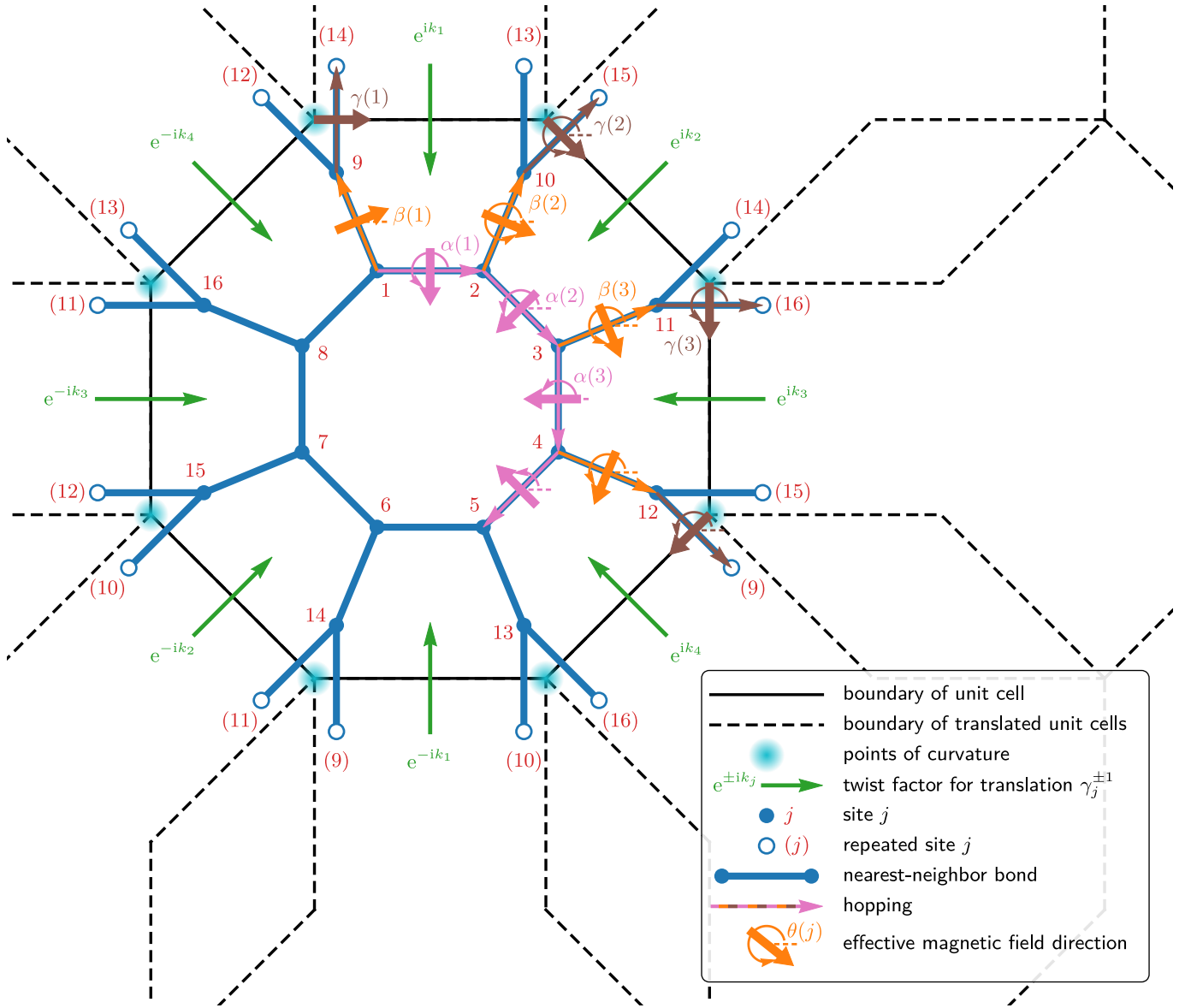
The advantage of the deformed model is that the NN hopping of electrons occurs within regions of zero curvature, allowing us to construct the Rashba SOC terms using the procedure familiar from the flat Euclidean space. Namely, we imagine the presence of a substrate that creates a constant electric field E_z perpendicular to the 2D plane of the system. As the spinful electron hops (within the locally flat region) between a pair of NN sites $b \leftarrow a$ (represented in Supplementary Fig. S1 with thin pink/orange/brown arrows), characterized by displacement vector $\mathbf{r}_{ba} = \mathbf{r}_b - \mathbf{r}_a$ [where the vectors are decomposed into local (x, y) coordinates that run rightwards/upwards inside the illustration in Supplementary Fig. S1], the electron perceives in its moving reference frame a magnetic field $\mathbf{B}_{ba} \propto \mathbf{r}_{ba} \times \mathbf{E}$ [where $\mathbf{E} = (0, 0, E_z)$, and \mathbf{r}_{ba} has been supplemented with vanishing component in the third direction]. The obtained magnetic fields are in-plane vectors [indicated for several hopping processes in Supplementary Fig. S1 with thick pink/orange/brown arrows], which are characterized by their direction θ_{ba} . The corresponding Rashba term added to the rhKM Hamiltonian is

$$\mathcal{H}_{ba} = i\lambda_R [\cos(\theta_{ba})\sigma_x + \sin(\theta_{ba})\sigma_y]. \quad (\text{S12})$$

By repeating the above procedure for hopping $a \leftarrow b$, we find that $\mathcal{H}_{ab} = -\mathcal{H}_{ba}$, which is compatible with time-reversal symmetry $\mathcal{T} = i\sigma_y\mathcal{K}$.

In the corresponding code in the enclosed data repository [60] (see also Supplementary Note S11), we label the angles θ_{ba} as one of $\{\alpha(j), \beta(j), \gamma(j)\}_{j=1}^8$ (illustrated in pink/orange/brown in Supplementary Fig. S1); the three symbols distinguish respectively the Rashba terms on NN bonds (1) along the inner elementary (blue) octagon, (2) directed towards the corners of the large (black) octagon, and (3) crossing the boundary of the large octagon.

Let us emphasize that the interpretation with the non-homogeneous curvature is only adopted to *construct* the Hamiltonian elements in Eq. (S12). When discussing the geometry of the system in the subsequent text, we still assume the 16 sites of the inner Bolza cell to be located at the complex coordinates listed in Supplementary Table S1, while keeping the Hamiltonian elements derived above.



Supplementary Figure S1. **Geometry of the reduced Kane-Mele model.** (For details of the construction, see Methods). In the reduced hyperbolic Kane-Mele model, the lattice is deformed such that all the negative curvature is concentrated at the corners (cyan dots) of the unit cell (the Bolza cell; deformed into the black octagon). As a consequence, space is flat everywhere except at those points (octagon corners,) and the neighbouring unit cells (dashed black octagons) seem to overlap in our representation of the lattice. The unit cell contains 16 sites (blue dots labelled by red numbers). Assuming an electric field due to the substrate pointing out of the plane, hopping between two sites (pink, orange and brown thin arrows) leads to an effective magnetic field pointing in the direction of the corresponding thick arrow (of the same color). This direction is parametrized by an angle $\theta(j)$, where $\theta = \alpha, \beta, \gamma$ depending on whether the hopping is on the inner ring, in the radial direction, or across different Bolza unit cells, respectively, and $j \in \{1, \dots, 8\}$ enumerates those nearest-neighbour bonds. Assuming first that we set the alternating on-site potential to $M = 0$, the constructed model preserves time-reversal symmetry \mathcal{T} , the eightfold rotation symmetry with respect to the center of the Bolza cell (corresponding to symmetry ‘ R ’ in the Supplementary Material to Ref. [9]), the mirror symmetry with respect to lines connecting antipodal corners of the unit cell (symmetry ‘ S ’ in Ref. [9]), and the mirror symmetry with respect to lines connecting centers of antipodal edges of the unit cell (composition of R and S). However, the model breaks the threefold rotation symmetry with respect to any site of the $\{8, 3\}$ lattice (symmetry ‘ U ’ in Ref. [9]), as is apparent from the varying geometrical distortions of the six elementary (blue) octagons in the Bolza unit cell. The on-site $\pm M$ term further breaks R (but not \mathcal{T} and S) symmetry. [Note that in the main text we use symbol ‘ R ’ to indicate a $(\pi/2)$ -rotation around the center of the Bolza cell, whereas the same symbol is used by Ref. [9] to indicate a $(\pi/4)$ -rotation around the same point.]

Supplementary Note S4: Hyperbolic Bloch Hamiltonian.

To obtain the hyperbolic Bloch Hamiltonian $\mathcal{H}(\mathbf{k})$ from tight-binding Hamiltonian \mathcal{H} in position space, we replace the infinite lattice by a single Bolza cell with identified antipodal boundaries [pairs of colored edges in Fig. 1(a)] [9]. To implement the twisted boundary conditions, tunnelling amplitudes (t) for hopping process that cross edges displaced by $\gamma_j^{\pm 1}$ are multiplied by phase factors $e^{\pm ik_j}$. Since there are four phases $\{k_j\}_{j=1}^4 \equiv \mathbf{k}$, it follows that $\mathcal{H}(\mathbf{k})$ is defined over a 4D BZ. For models on the $\{8, 3\}$ lattice, the presence of $n_{\text{cell}}=16$ sites per Bolza cell implies that $\mathcal{H}(\mathbf{k})$ is a matrix of dimensions $D_{\text{Bloch}}=n_{\text{cell}}$ ($D_{\text{Bloch}} = 2n_{\text{cell}}$) in the absence (presence) of the spin degree of freedom [49]Urwyler:2022b. The Bloch Hamiltonians for the studied models are constructed in Supplementary Note S11), and made available as MATHEMATICA notebooks in the data repository [60].

We further consider the generation of density from HBT. Given a hyperbolic Bloch Hamiltonian, we perform random sampling of N_k momenta over the 4D hypercubic BZ, $\forall j \in \{1, 2, 3, 4\} : k_j \in [-\pi, \pi]$. The collected list of eigenvalues $\{\varepsilon_j\}_{j=1}^{N_k D_{\text{Bloch}}}$ is converted into a continuous DoS function via

$$\rho^{\text{HBT}}(E) = \frac{1}{N_k D_{\text{Bloch}}} \sum_{j=1}^{N_k D_{\text{Bloch}}} f_{\eta}(E - \varepsilon_j) \quad (\text{S13})$$

where $f_{\eta}(\varepsilon) = \frac{1}{\eta\sqrt{2\pi}} \exp\left[-\frac{\varepsilon^2}{2\eta^2}\right]$ is a Gaussian smearing function. The factor in front of the summation symbol is chosen such that $\rho^{\text{HBT}}(E)$ integrates to 1. We use $\eta = 0.063$ and $N_k = 2 \times 10^4$ throughout the manuscript.

Supplementary Note S5: Flake Hamiltonian in position space.

Two inputs are used to algorithmically construct the lattice Hamiltonian $\mathcal{H}^{\text{flake}}$ on a circular-flake in position space: the hyperbolic Bloch Hamiltonian $\mathcal{H}(\mathbf{k})$, and the target number \tilde{N}_{UC} of unit cells. The Bloch Hamiltonian has components $\mathcal{H}(\mathbf{k}) = \{h_{ab}(\mathbf{k})\}_{a,b=1}^{n_{\text{cell}}}$. For the models presented in this work, one finds that $h_{ab}(\mathbf{k}) = t_{ab}e^{ik \cdot \mathbf{e}_{ab}}$ with a unique value of the 4-component vector \mathbf{e}_{ab} and of the hopping amplitude t_{ab} for each $a, b \in \{1, \dots, n_{\text{cell}}\}$. (Note that here we treat t_{ab} as a single complex number for spinless models, and as a complex-valued 2×2 matrix for spinful models.) The algorithm, which is implemented in the data repository [60], proceeds in the following steps.

First, we invert Eq. (S11) to determine an estimated radius $R(\tilde{N}_{\text{UC}}) = [\tilde{N}_{\text{UC}}/(1 + \tilde{N}_{\text{UC}})]^{1/2}$ of a disk in the complex plane that contains \tilde{N}_{UC} Bolza cells. We center one of the Bolza cells at $z = 0$, and we use the known action ρ_{γ_j} of generators γ_j on the complex coordinates in \mathbb{D} [Eq. (45) in Ref. 13] to identify the centers of all cells of the $\{8, 8\}$ (Bolza) lattice that lie within the distance $R(\tilde{N}_{\text{UC}})$ from the origin. (Note that the centers of the Bolza cells do not coincide with any site of the $\{8, 3\}$ lattice.) This results in a *list of Bolza cells*, $L_{\text{cells}} = \{w_\ell\}_{\ell=1}^{N_{\text{UC}}}$; here, each w_ℓ is a sequence of generators and their inverses (a ‘‘word’’) that translates $z = 0$ to $\rho_{w_\ell}(0) = z_j$ within the disk of radius R (i.e., $|z_j| < R$), and N_{UC} is the total number of selected Bolza cells. The words w_ℓ are elements of the hyperbolic translation group, and act on complex coordinates inside the Poincaré disk by ρ_{w_ℓ} , which is the corresponding composition of ρ_{γ_j} (and of their inverses). The word ‘ \emptyset ’ of length zero (which corresponds to the identity of the translation group) is always present in L_{cells} ; it encodes the Bolza cell centered at $z = 0$. We then apply L_{cells} to generate a *list of sites* of the $\{8, 3\}$ lattice, $\tilde{L}_{\text{sites}} = \{(w_\ell, a)\}$, where $1 \leq a \leq n_{\text{cell}}$ labels the individual sites within each Bolza cell $w_\ell \in L_{\text{cells}}$. The complex coordinates of the sites are obtained as $z_{(w_\ell, a)} = \rho_{w_\ell}(z_{(\emptyset, a)})$.

We next use the list \tilde{L}_{sites} and the amplitudes t_{ab} to construct the real-space Hamiltonian $\tilde{\mathcal{H}}^{\text{flake}}$. The Hamiltonian has $\tilde{n}_{\text{flake}} \times \tilde{n}_{\text{flake}}$ components, where $\tilde{n}_{\text{flake}} = n_{\text{cell}}N_{\text{UC}}$ is the length of list \tilde{L}_{sites} . Since the presently considered tight-binding Hamiltonians contain only NN and NNN terms, we run the following routine. For each pair (x, y) with $x = (w_\ell, a)$ and $y = (w_m, b)$ in \tilde{L}_{sites} , compute the distance $d(z_x, z_y)$. If the distance is equal to the NN distance $d_1^{\{8,3\}}$ or to the NNN distance $d_2^{\{8,3\}}$, we set $(\tilde{\mathcal{H}}^{\text{flake}})_{x,y} = t_{ab}$. In the very last step, we smooth the boundary of the system by identifying sites that have only a single NN. We drop the corresponding rows and columns of $\tilde{\mathcal{H}}^{\text{flake}}$, which results in the final Hamiltonian $\mathcal{H}^{\text{flake}}$ that has a slightly decreased number of components $n_{\text{flake}} \times n_{\text{flake}}$ (we similarly define the corresponding shortened list of sites L_{sites} of length n_{flake}). Note that for spinful models, the counted Hamiltonian components are 2×2 blocks, i.e., the actual Hamiltonian dimension is $D_{\text{flake}} = n_{\text{flake}}$ ($D_{\text{flake}} = 2n_{\text{flake}}$) for spinless (spinful) models.

Supplementary Note S6: Considered system sizes in the flake geometry.

The assumed system size varies between the figures. We encode the size for each calculation with the triplet “SIZE = $(\widetilde{N}_{UC}, N_{UC}, n_{flake})$ ” (where N_{UC} and n_{flake} are selected automatically by the above-outlined algorithm upon inputting \widetilde{N}_{UC}).

For the hH model, the sizes are set up as follows:

- Fig. 1(b,c) and Fig. 2(c): SIZE = (700, 761, 8496),
- Supplementary Fig. S2(a,c) and Supplementary Fig. S4(a): SIZE = (400, 409, 4520),
- Fig. 4(a) and Supplementary Fig. S7(b): SIZE = (500, 569, 6344 \mapsto 896),
- Fig. 4(b,c) and Supplementary Fig. S4(b,c): SIZE = (200, 169, 1864).

For the rhKM model, we chose the following sizes:

- Supplementary Fig. S2(a,d) and Supplementary Fig. S3: SIZE = (200, 169, 1864),
- Fig. 3(b) and Fig. 5: SIZE = (300, 297, 3304),
- Supplementary Fig. S7(b): SIZE = (500, 569, 6344 \mapsto 896).

Note that in the calculations leading to Fig. 4(a) and to Supplementary Fig. S7(a,b), an additional level of removing sites at the boundary is applied, namely, starting with the list \widetilde{L}_{sites} , we remove all sites with less than three nearest neighbors. Thus, instead of arriving at a system with 6344 sites, we obtain a much smaller system with 896 sites, cf. Supplementary Note S13.

Supplementary Note S7: Bulk density of states and integrated boundary density of states for the flake Hamiltonian.

Given a lattice Hamiltonian $\mathcal{H}^{\text{flake}}$ on a circular flake, we perform ED to find its eigensystem $\Lambda^{\text{flake}} = \{(E_j, |\phi_j\rangle)\}_{j=1}^{D_{\text{flake}}}$, where $|\phi_j\rangle$ is an eigenvector with eigenvalue E_j . Each eigenstate is a list of amplitudes, namely $|\phi_j\rangle = \{\phi_{j,x}\}_{x \in L_{\text{sites}}}$ for spinless models ($|\phi_j\rangle = \{\phi_{j,x,\sigma}\}_{x \in L_{\text{sites}}, \sigma \in \{\uparrow, \downarrow\}}$ for spinful models). For each state we define the *bulk weight* ϖ_j as the probability that the particle in such a state is located on the innermost unit cell (i.e., sites with $w_\ell = \emptyset$),

$$\varpi_j^{\text{bulk}} = \sum_{a=1}^{16} |\phi_{j,(\emptyset,a)}|^2 \quad \text{and} \quad \varpi_j^{\text{bulk}} = \sum_{a=1}^{16} \sum_{\sigma \in \{\uparrow, \downarrow\}} |\phi_{j,(\emptyset,a),\sigma}|^2 \quad (\text{S14})$$

for spinless and spinful models, respectively. We then convert the information about the eigenvalues and eigenvectors into a continuous DoS function via

$$\rho_{\text{bulk}}^{\text{ED}}(E) = \frac{1}{D_{\text{Bloch}}} \sum_{j=1}^{D_{\text{flake}}} \varpi_j^{\text{bulk}} f_\eta(E - E_j) \quad (\text{S15})$$

with the smearing function f_η defined below Eq. (S13). The prefactor $1/D_{\text{Bloch}}$ guarantees that $\rho_{\text{bulk}}^{\text{ED}}(E)$ integrates to 1. To achieve a simple comparison with the HBT data, we use $\eta = 0.063$ throughout the manuscript.

We next define the integrated DoS at the boundary in analogy with Eq. (S15), where the only difference is the replacement $\varpi_j^{\text{bulk}} \mapsto \varpi_j^{\text{bound.}}$, with

$$\varpi_j^{\text{bound.}} = \sum_{x \in L_{\text{bound.}}} |\phi_{j,x}|^2 \quad \text{and} \quad \varpi_j^{\text{bound.}} = \sum_{x \in L_{\text{bound.}}} \sum_{\sigma \in \{\uparrow, \downarrow\}} |\phi_{j,x,\sigma}|^2 \quad (\text{S16})$$

for spinless and spinful models, respectively, where $L_{\text{bound.}}$ is a sublist of L_{sites} that selects sites with two nearest neighbors.

Supplementary Note S8: Real-space invariants.

For the energy gap at chemical potential μ , we compute the *real-space Chern number* using the formula from Ref. 39,

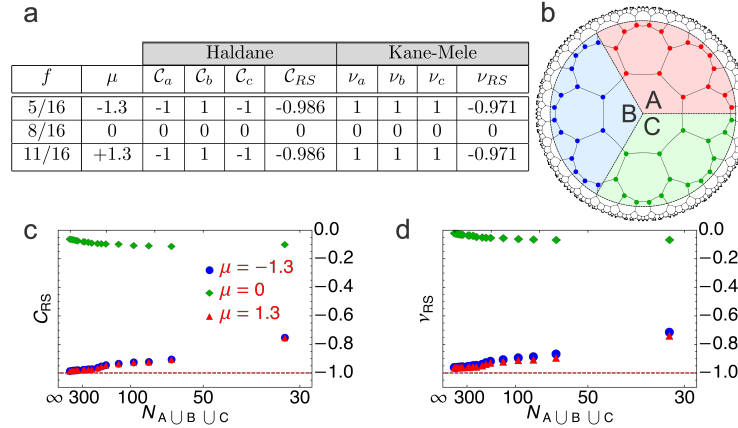
$$C_{RS}(\mu) = 12\pi i \sum_{j \in A} \sum_{k \in B} \sum_{\ell \in C} \left(\mathbb{P}_{jk}^{\mu} \mathbb{P}_{k\ell}^{\mu} \mathbb{P}_{\ell j}^{\mu} - \mathbb{P}_{j\ell}^{\mu} \mathbb{P}_{\ell k}^{\mu} \mathbb{P}_{kj}^{\mu} \right) \quad (\text{S17})$$

where \mathbb{P}^{μ} is the projector onto the subspace of occupied single-particle states at chemical potential μ , and A, B, C are three regions in the bulk of the systems that (i) *do not* extend all the way to the boundary, and which (ii) are arranged counter-clockwise around the center of the system [cf. Fig. S2(b)].

In the presence of time-reversal symmetry, we compute the *real-space spin Chern number* ν_{RS} following the ideas of Refs. 41 and 42. Namely, we first construct the *projected spin operator* $\mathbb{P}_z^{\mu} = \mathbb{P}^{\mu} \sigma_z \mathbb{P}^{\mu}$. Next, we perform spectral decomposition of the projected spin operator into eigenstates ($|\zeta_j\rangle$) and eigenvalues (S_j). As long as the spin-mixing Rashba term is weak, the eigenvalues S_j remain close to ± 1 , allowing us to define the index sets \mathfrak{S}_{\pm} ; in addition, there are unphysical zero eigenvalues, which correspond to the part of the Hilbert space that is projected out by \mathbb{P}^{μ} . This allows us to define projectors $\mathbb{P}_{\pm} = \sum_{j \in \mathfrak{S}_{\pm}} |\zeta_j\rangle \langle \zeta_j|$. The integer-valued real-space spin Chern number is then obtained as

$$\nu_{RS}(\mu) = \frac{1}{2} \left[\nu_{RS}^+(\mu) - \nu_{RS}^-(\mu) \right], \quad (\text{S18})$$

where $\nu_{RS}^{\pm}(\mu)$ are computed per Eq. (S17) with replaced $\mathbb{P}^{\mu} \mapsto \mathbb{P}_{\pm}^{\mu}$. Note that for strong SOC, the eigenstates of \mathbb{P}_z no longer exhibit a clear spectral gap between the two sets \mathfrak{S}_{\pm} , and the formula in Eq. (S18) ceases to be applicable. We verified that this issue does not arise for our selected model parameters.



Supplementary Figure S2. **Topological invariants.** **a.** Summary of topological invariants for the hyperbolic Haldane and reduced hyperbolic KM models for their respective three energy gaps, labelled by filling fraction f and chemical potential μ . We show both momentum-space band invariants (subscripts a and b) and real-space topological markers (subscript RS) **b.** Regions A, B, C involved in the computation of the real-space invariants. **c, d.** Convergence of the computed real-space Chern number (**c**) and real-space spin Chern number (**d**) for the three energy gaps (labelled by μ) upon increasing the size of the regions A, B, C. Here N_{AUBUC} is the total number of sites in the three regions.

Haldane/ Kane-Mele										
N_{AUBUC}	16	32	64	80	96	120	152	168	184	216
$C_{RS} (\mu = \pm 1.3)$	-0.661	-0.751	-0.904	-0.921	-0.924	-0.934	-0.944	-0.953	-0.962	-0.972
$\nu_{RS} (\mu = -1.3)$	-0.638	-0.723	-0.876	-0.895	-0.903	-0.916	-0.926	-0.937	-0.948	-0.955
$\nu_{RS} (\mu = +1.3)$	-0.654	-0.747	-0.902	-0.915	-0.918	-0.929	-0.937	-0.945	-0.955	-0.964
N_{AUBUC}	240	272	288	368	400	448	496	544	624	
$C_{RS} (\mu = \pm 1.3)$	-0.973	-0.976	-0.976	-0.979	-0.980	-0.981	-0.982	-0.984	-0.986	
$\nu_{RS} (\mu = -1.3)$	-0.957	-0.963	-0.963	-0.966	-0.966	-0.968	-0.969	-0.971	-0.970	
$\nu_{RS} (\mu = +1.3)$	-0.965	-0.967	-0.968	-0.969	-0.969	-0.970	-0.971	-0.971	-0.970	

Supplementary Table S2. **Tabulated values of data in Fig. S2(c,d).** The values indicate the convergence of the topological markers in positions space to values ± 1 as the number of sites N_{AUBUC} in the summation region is increased.

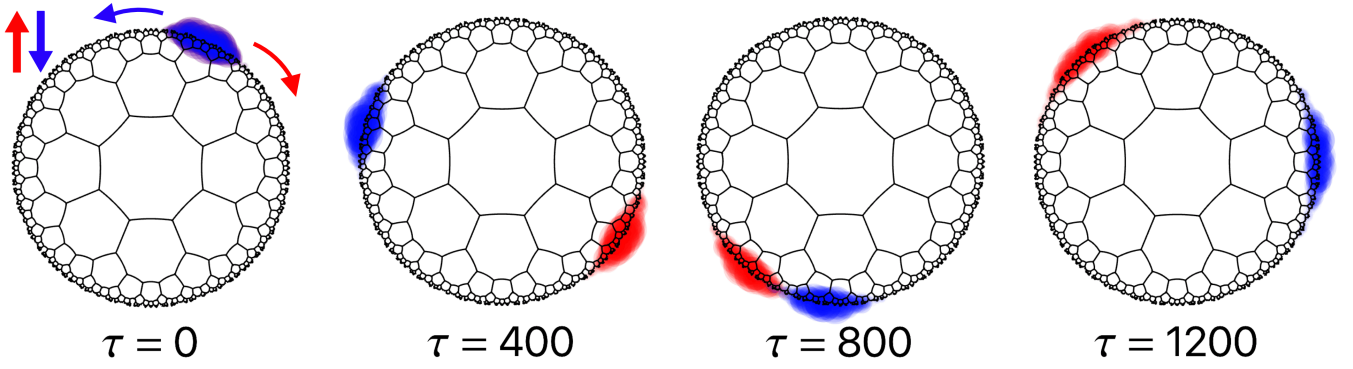
[4]

Supplementary Note S9: Gaussian projector operator.

Given the eigensystem of a flake Hamiltonian, $\Lambda^{\text{flake}} = \{(E_j, |\phi_j\rangle)\}_{j=1}^{D_{\text{flake}}}$, we construct for an energy range $[\mu - \sigma, \mu + \sigma]$ within a topological energy gap the operator

$$\mathbb{P}_{(\mu, \sigma)} = \sum_{j=1}^{D_{\text{flake}}} \exp\left[-\frac{(E_j - \mu)^2}{2\sigma^2}\right] |\phi_j\rangle\langle\phi_j|. \quad (\text{S19})$$

Note that $\mathbb{P}_{(\mu, \sigma)}$ is not a projector in the traditional sense, since its eigenvalues are arbitrary numbers in range $[0, 1]$. The idea behind the exponential weight factor in Eq. (S19) is that, per the approximately linear dispersion of the edge state visible in Fig. 4(a), we construct a Gaussian function in angular momentum ℓ . Therefore, the wave function $\mathbb{P}_{(\mu, \sigma)} |\varphi_{\text{site}}\rangle$ has approximately Gaussian coefficients in its decomposition to angular momenta, implying it constitutes a Gaussian wave packet in the angular coordinate α .



Supplementary Figure S3. **Propagation of edge states in the rhKM model.** We compute and plot the propagation of helical edge states around the boundary of a flake supporting the rhKM model. The time evolution is computed according to the description in section ‘*Bulk-boundary correspondence*’ of the main text, and we use the Gaussian projector $\mathbb{P}_{(\mu, \sigma)}$ with $(\mu, \sigma) = (1.3, 0.025)$. The indicated time τ is counted in multiples of $1/t_1$. The initial single-site localized state $|\varphi_{\text{site}}\rangle$ was chosen to have the form $\frac{1}{\sqrt{2}}(1, 1)^T$ in the spin degree of freedom. We observe that time-evolution splits $\mathbb{P}_{(\mu, \sigma)} |\varphi_{\text{site}}\rangle$ into a pair of counter-propagating wave packets that during the time evolution pass through one another without scattering.

Supplementary Note S10: Models of disorder.

For the hH Hamiltonian $\mathcal{H}_{\text{hH}}^{\text{flake}}$, we consider the addition of random on-site potential, i.e., for each site a we add to $(\mathcal{H}_{\text{hH}}^{\text{flake}})_{aa}$ a random value drawn from the box distribution bounded by $\pm W_{\text{max}}$.

For the rhKM Hamiltonian $\mathcal{H}_{\text{rhKM}}^{\text{flake}}$, we consider the addition of a random spin-dependent term to each pair (a, b) of NN and NNN sites. We specifically consider terms that are off-diagonal in the spin-degree of freedom; namely, for each pair (a, b) we draw random values $\alpha_{x,y} \in [-W_{\text{max}}, +W_{\text{max}}]$, and increase the 2×2 Hamiltonian blocks as follows:

$$\text{TR-symmetric disorder : } (\mathcal{H}_{\text{rhKM}}^{\text{flake}})_{ab} += i(\alpha_x \sigma_x + \alpha_y \sigma_y), \quad (\text{S20})$$

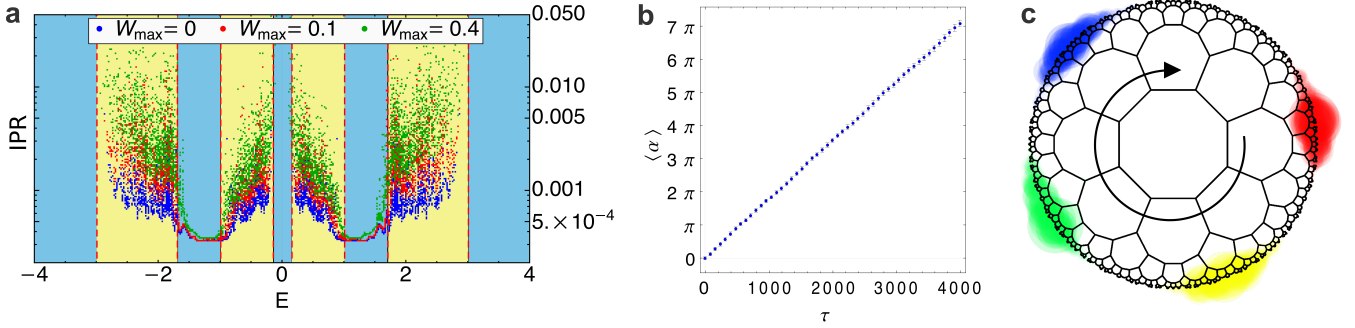
$$\text{TR-breaking disorder : } (\mathcal{H}_{\text{rhKM}}^{\text{flake}})_{ab} += (\alpha_x \sigma_x + \alpha_y \sigma_y), \quad (\text{S21})$$

with $(\mathcal{H}_{\text{rhKM}}^{\text{flake}})_{ba} = (\mathcal{H}_{\text{rhKM}}^{\text{flake}})_{ab}^\dagger$ for both cases. The disorder in Eq. (S20) is interpretable as random Rashba SOC, while the one in Eq. (S21) corresponds to random in-plane magnetic fields along the trajectory connecting sites (a, b) .

The localization of a normalized eigenstate $|\phi_j\rangle$ is quantified by the inverse participation ratio, defined for spinless and spinful systems as

$$\text{IPR}_j = \sum_{a=1}^{n_{\text{flake}}} |\phi_{j,a}|^4 \quad \text{resp.} \quad \text{IPR}_j = \sum_{a=1}^{n_{\text{flake}}} (|\phi_{j,a,\uparrow}|^2 + |\phi_{j,a,\downarrow}|^2)^2. \quad (\text{S22})$$

One easily verifies that if $|\phi_j\rangle$ were homogeneously distributed over N sites, then $\text{IPR}_j = 1/N$. This implies the interpretation that an eigenstate characterized by IPR_j as being distributed over approximately $1/\text{IPR}_j$ sites.



Supplementary Figure S4. **Robustness against Anderson disorder in the hyperbolic Haldane model.** The disorder chosen for the hyperbolic Haldane model corresponds to the addition of a random on-site potential drawn from a box distribution in range $[-W_{\text{max}}, W_{\text{max}}]$. **a**, IPR of the individual eigenstates for various choices of disorder strength W_{max} . Note that the domain of low values of IPR has reduced to a narrower range of energies for the green data ($W_{\text{max}} = 0.4$), indicating the shrinking of the bulk energy gap; nevertheless, the robustness of edge states with low IPR is manifest. **b–c**, Propagation of chiral edge states in disordered hH model. The calculation is analogous to Fig. 4(b,c) of the main text, but here we assume the addition of a strong random on-site potential with disorder strength $W_{\text{max}} = 0.4$ (green in panel a). The wave packet continues to propagate around the flake boundary with nearly uniform angular velocity. The parameters of the Gaussian projector are $(\mu, \sigma) = (1.3, 0.025)$, and the data in red/yellow/green/blue color consecutively correspond to the wave packet at times $\tau = (0, 240, 480, 720)$, $(\mu, \sigma) = (1.3, 0.025)$.

Supplementary Note S11: Hyperbolic Bloch Hamiltonians of the studied models

Since the hyperbolic Bloch Hamiltonians $\mathcal{H}(\mathbf{k})$ studied in this work are 16×16 and 32×32 matrices, we do not write them explicitly. Instead, we include here the MATHEMATICA code that generates these Hamiltonians when compiled (the corresponding MATHEMATICA notebooks are included in the data repository [60]).

We first specify the following:

```
$Assumptions = {
  k1 \[Element] Reals, k2 \[Element] Reals,
  k3 \[Element] Reals, k4 \[Element] Reals,
  t1 \[Element] Reals, t2 \[Element] Reals,
  flux \[Element] Reals, M \[Element] Reals, LR \[Element] Reals
};

kList = {k1, k2, k3, k4, -k1, -k2, -k3, -k4};
```

The hyperbolic Bloch Hamiltonian of the NN model on the $\{8, 3\}$ lattice is obtained as Hnn with the following code:

```
Hnn = ConstantArray[0, {16, 16}];

For[a = 1, a < 9, a++,
  Hnn[[Mod[a, 8] + 1, a]] = t1;
  Hnn[[a + 8, a]] = t1;
  Hnn[[8 + Mod[a + 4, 8] + 1, 8 + a]] = t1*Exp[-I*kList[[a]]];
];

Hnn = FullSimplify[Hnn + ConjugateTranspose[Hnn]];
```

After including the mass term, we obtain the hyperbolic Bloch Hamiltonian $\mathcal{H}_{\{8,3\}}(\mathbf{k})$ as H83 with the following code:

```
Hmass = ConstantArray[0, {16, 16}];
For[a = 1, a < 9, a++,
  Hmass[[a, a]] += M*Power[-1, a + 1];
  Hmass[[a + 8, a + 8]] += -M*Power[-1, a + 1];
];

H83 = Hnn + Hmass;
```

To obtain the hyperbolic Bloch Hamiltonian $\mathcal{H}_{\text{hH}}(\mathbf{k})$ for the hyperbolic Haldane model, encoded as Hh in the code below, we further define a matrix Hflux of NNN terms.

```
Hflux = ConstantArray[0, {16, 16}];

For[a = 1, a < 9, a++,
  Hflux[[Mod[a + 1, 8] + 1, a]] = t2*f;

  Hflux[[a, 8 + Mod[a, 8] + 1]] = t2*f;
  Hflux[[8 + Mod[a - 2, 8] + 1, a]] = t2*f;

  Hflux[[8 + Mod[a + 4, 8] + 1, a]] = t2*f*Exp[-I*kList[[a]]];
  Hflux[[a, 8 + Mod[a + 2, 8] + 1]] =
  t2*f*Exp[I*kList[[Mod[a - 2, 8] + 1]]];

  Hflux[[8 + Mod[a + 2, 8] + 1, 8 + Mod[a + 4, 8] + 1]] =
  t2*f*Exp[I*(kList[[a]] - kList[[Mod[a - 2, 8] + 1]])];
];

Hflux = FullSimplify[Hflux + ConjugateTranspose[Hflux]];

Hh = FullSimplify[H83 + Hflux /. f \[Rule] Exp[I*flux]];
```

We next proceed to construct the hyperbolic Bloch Hamiltonian $\mathcal{H}_{\text{rhKM}}(\mathbf{k})$ of the reduced hyperbolic Kane-Mele model. To that end, we first double the Haldane model into a ‘quantum spin Hall’ Hamiltonian Hqsh :

```
Hqsh = ArrayFlatten[
  {
    {(H83 + Hflux) /. f \[Rule] Exp[I*flux]}, 0},
    {0, (H83 + Hflux) /. f \[Rule] Exp[\[Minus]I*flux]}
  }
];
```

The spin-orbit-coupled rhKM model is finally obtained as Hhkm with the following code:

```
Hsoc = ConstantArray[0, {16, 16}];

For[a = 1, a < 9, a++,
  alpha = -Pi/2 - (a - 1)*(2 Pi/8);
  Hsoc[[Mod[a, 8] + 1, a]] = I*(Cos[alpha]*PauliMatrix[1] + Sin[alpha]*PauliMatrix[2]);
  Hsoc[[a, Mod[a, 8] + 1]] = -I*(Cos[alpha]*PauliMatrix[1] + Sin[alpha]*PauliMatrix[2]);

  beta = Pi/8 - (a - 1)*(2 Pi/8);
  Hsoc[[a + 8, a]] = I*(Cos[beta]*PauliMatrix[1] + Sin[beta]*PauliMatrix[2]);
  Hsoc[[a, a + 8]] = -I*(Cos[beta]*PauliMatrix[1] + Sin[beta]*PauliMatrix[2]);

  gamma = 0 - (a - 1)*(2 Pi/8);
  Hsoc[[8 + Mod[a + 4, 8] + 1, 8 + a]] =
  I*(Cos[gamma]*PauliMatrix[1] + Sin[gamma]*PauliMatrix[2])*Exp[-I*kList[[a]]];
  Hsoc[[8 + a, 8 + Mod[a + 4, 8] + 1]] =
  -I*(Cos[gamma]*PauliMatrix[1] + Sin[gamma]*PauliMatrix[2])*Exp[I*kList[[a]]];
];

For[a = 1, a < 17, a++,
  For[b = 1, b < 17, b++,
    If[Hsoc[[a, b]] == 0,
      Hsoc[[a, b]] = ConstantArray[0, {2, 2}];
    ];
  ];
];

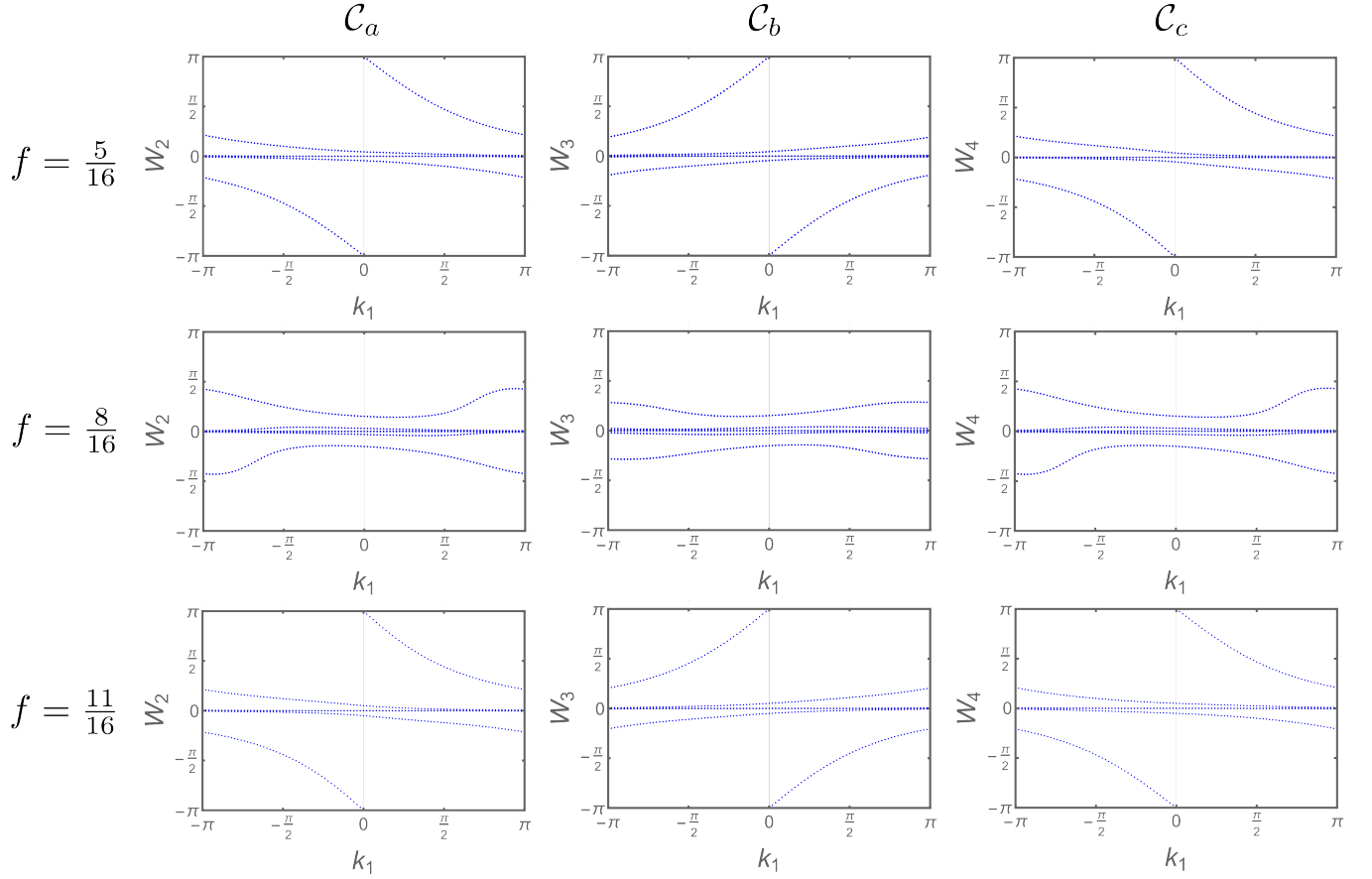
Hsoc = ArrayFlatten@Transpose[Hsoc, {3, 4, 1, 2}];

Hhkm = (Hqsh /. flux \[Rule] Pi/2) + LR*Hsoc;
```

Supplementary Note S12: Wilson-loop extraction of topological band invariants

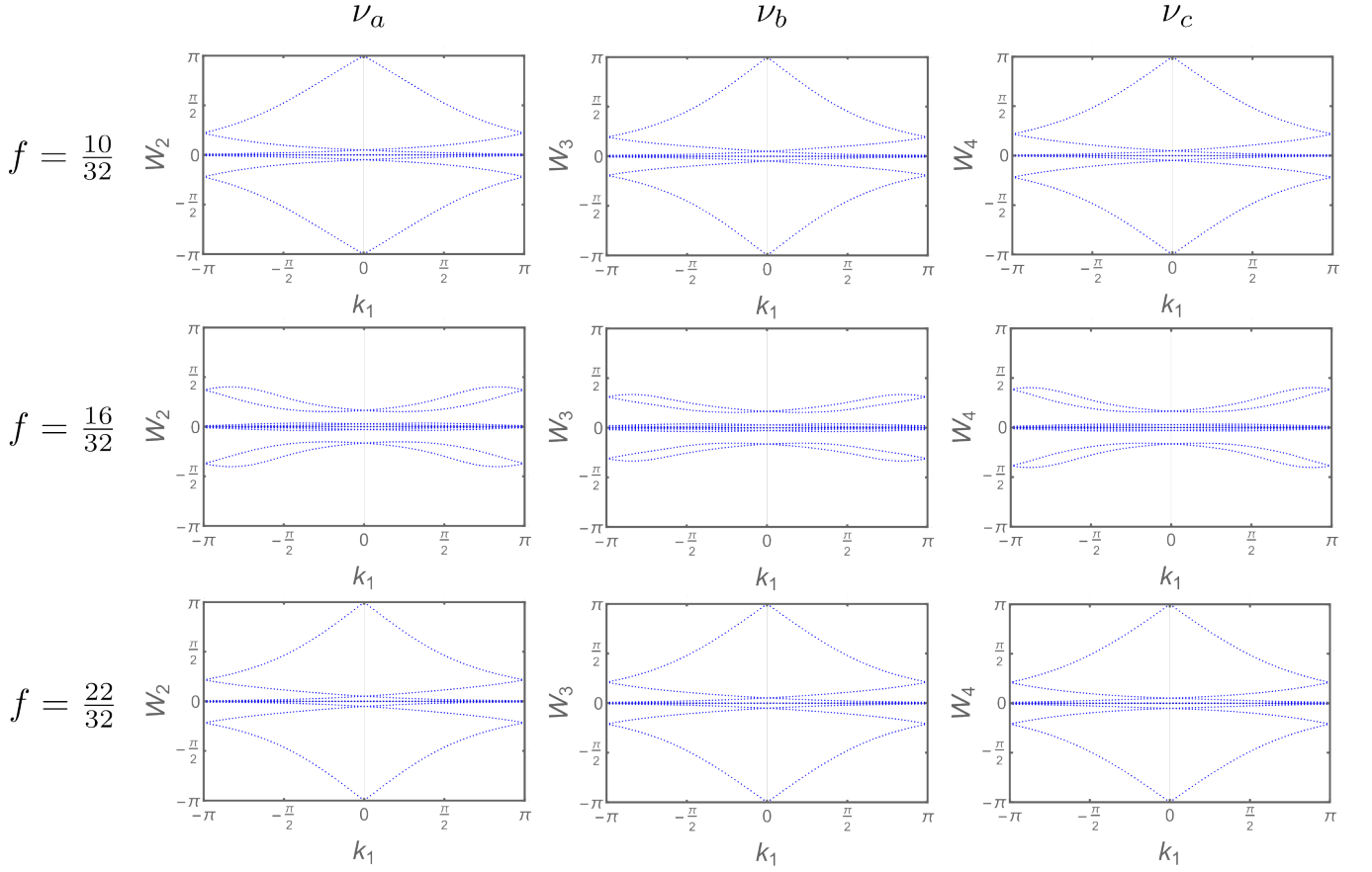
We extract topological band invariants of hyperbolic Bloch Hamiltonians on two-dimensional planes in the 4D BZ using the Wilson-loop technique [50, 51]. The utilized code is shared in the data repository [60].

First, we determine the Chern numbers $C_a, C_b, C_c \in \mathbb{Z}$ of the hyperbolic Haldane model $\mathcal{H}_{\text{hH}}(\mathbf{k})$ by computing the Wilson loop in the k_2 -, k_3 - resp. k_4 -direction (labelled as W_2, W_3 , resp. W_4) as a function of k_1 . The results of our analysis are shown in Fig. S5, and tabulated in Fig. S2(a).



Supplementary Figure S5. **Wilson-loop spectra for the hH model.** Rows represent the three energy gaps of the model at the indicated filling fractions f , while columns correspond to the three pairs of planes that we do not relate by symmetry in the discussion in the main text. The Wilson spectra reveal the values of the Chern numbers tabulated in Fig. S2(a). Note that the number of plotted Wilson bands matches the number of filled energy bands (numerators of f); however, some of the bands are not resolved since they coincide close to zero value.

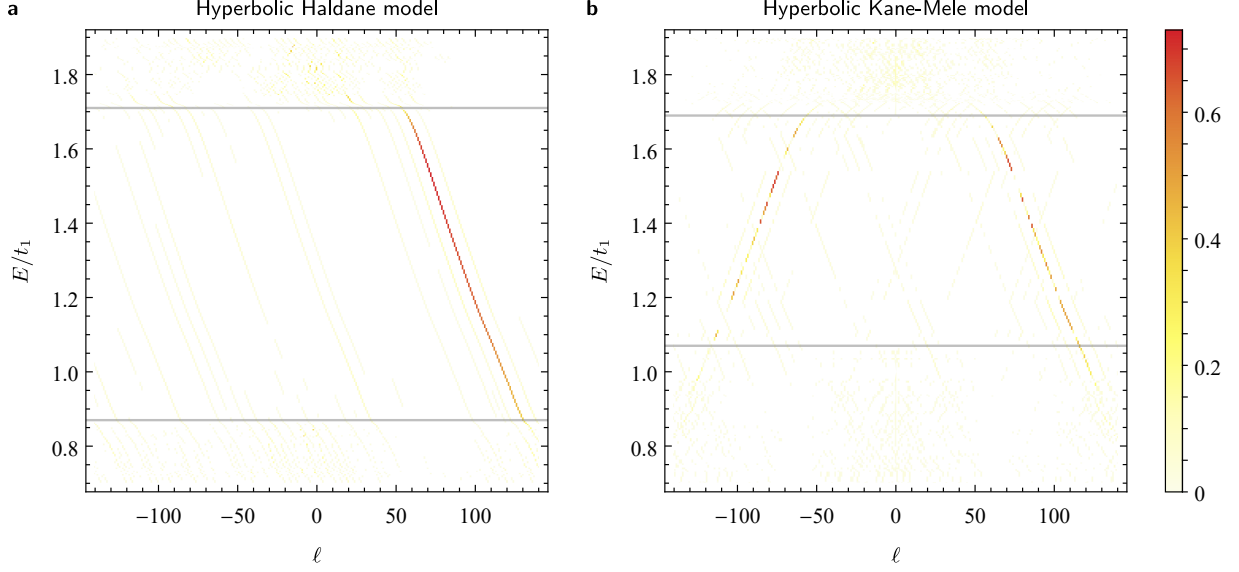
We next determine the Kane-Mele invariants $\nu_a, \nu_b, \nu_c \in \mathbb{Z}_2$ for the reduced hyperbolic Kane-Mele model $\mathcal{H}_{\text{thKM}}(\mathbf{k})$ by computing the Wilson loop in the k_2 -, k_3 - resp. k_4 -direction (labelled again as W_2, W_3 , resp. W_4) as a function of k_1 . The results of our analysis are shown in Fig. S6.



Supplementary Figure S6. **Wilson-loop spectra for the rhKM model.** Rows represent the three energy gaps of the model at the indicated filling fractions f , while columns correspond to the three pairs of planes that we do not relate by symmetry in the discussion in the main text. The Wilson spectra reveal the values of the Kane-Mele invariants tabulated in Fig. S2(a). The number of plotted Wilson bands matches the number of filled energy bands (numerators of f); however, some of the bands are not resolved since they coincide close to zero value.

Supplementary Note S13: Extraction of the edge mode dispersion

In this supplementary note we describe a method we developed to determine the angular momentum of a given eigenstate of the Hamiltonian defined on a hyperbolic lattice. This method is used to generate the data for the dispersion of the chiral edge state of the hH model plotted in Fig. 4a of the main text.



Supplementary Figure S7. **Angular momentum dispersion of edge modes.** Contribution ϕ_ℓ [cf. Eq. (S39) in Supplementary Note S13] of different angular momenta to the states lying in the upper energy gap for **a**, the Haldane model, and **b**, the reduced Kane-Mele model defined on the flake of the $\{8, 3\}$ lattice shown in Supplementary Fig. S9. The horizontal grey lines indicate the band edges below and above the gap, and were determined from the density of states $\rho_{\text{bulk}}^{\text{ED}}$ for the here considered system size. **a**, In the Haldane model, there is a single (chiral) propagating edge mode with a very sharp angular momentum dispersion lying exactly in the gap. **b**, In the case of the Kane-Mele model, we find in the gap two (helical) counter-propagating edge modes. The two edge-state branches are characterized by opposite sign of the angular momentum (ℓ) as well as of the angular momentum dispersion ($dE/d\ell$).

The method relies on a decomposition of functions defined on the disk $\mathbb{D}_R = \{z \in \mathbb{C} \mid |z| \leq R\}$ of radius $0 < R < 1$ with the hyperbolic metric given by Eq. (S1) into eigenmodes of the Laplace-Beltrami operator

$$\Delta = (1 - |z|^2)^2 \left(\frac{\partial^2}{\partial x^2} + \frac{\partial^2}{\partial y^2} \right), \quad (\text{S23})$$

where $z = x + iy \in \mathbb{C}$. The solutions to the Dirichlet problem

$$(\Delta + \lambda)u(z) = 0, \quad u(z)|_{(z) \in \partial\mathbb{D}_R} = 0 \quad (\text{S24})$$

form an orthonormal basis for functions on \mathbb{D}_R and they are given [6, 13] by

$$u_{n,\ell}(z) = \frac{g_{k_n,\ell}(|z|)}{\|g_{k_n,\ell}\|} e^{i\ell \arg(z)}, \quad (\text{S25})$$

where

$$g_{k,\ell}(r) = \begin{cases} P_{\frac{1}{2}(-1+ik)}^0 \left(\frac{1+r^2}{1-r^2} \right), & \ell = 0 \\ \left(\prod_{m=0}^{\ell-1} \left(-\frac{1}{2} - m + ik \right) \right)^{-1} P_{\frac{1}{2}(-1+ik)}^\ell \left(\frac{1+r^2}{1-r^2} \right), & \ell > 0, \\ (-1)^\ell g_{k,|\ell|}(r), & \ell < 0 \end{cases} \quad (\text{S26})$$

$P_q^\ell(s)$ are the associated Legendre functions, $\|g\| = \sqrt{\langle g, g \rangle}$ is the norm induced by the inner product on \mathbb{D}_R

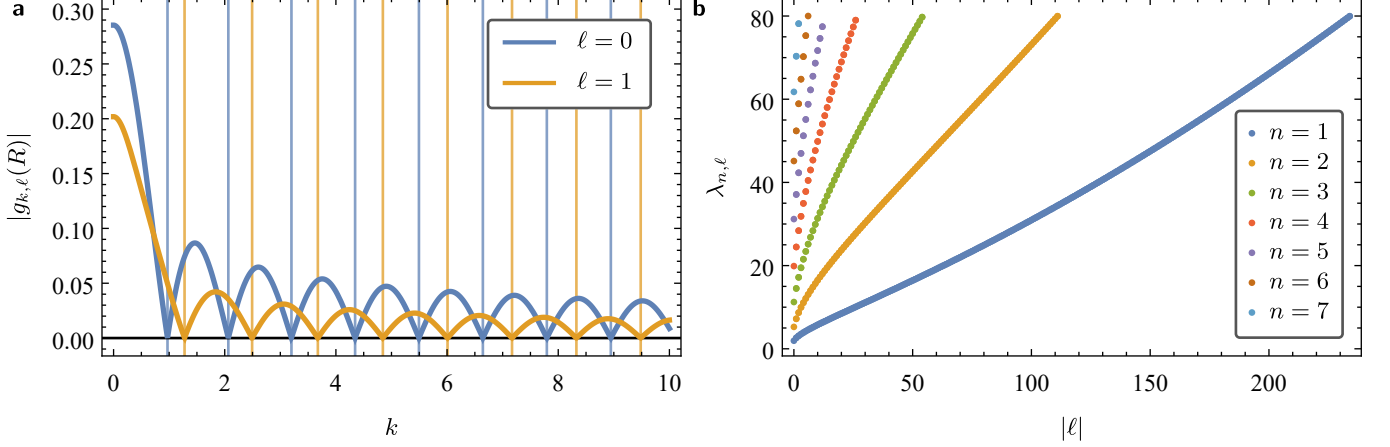
$$\langle v, w \rangle = \int_{|z| \leq R} \frac{d^2z}{(1 - |z|^2)^2} v(z)^* w(z), \quad (\text{S27})$$

$k_{n,\ell}$ is the n -th zero of

$$k \mapsto P_{\frac{1}{2}(-1+ik)}^\ell \left(\frac{1+R^2}{1-R^2} \right), \quad (\text{S28})$$

and $\ell \in \mathbb{Z}$. The solutions to Eq. (S28) correspond to zeroes of $g_{k,\ell}(R)$, cf. Supplementary Fig. S8a.

For the flake of the $\{8, 3\}$ lattice shown in Supplementary Fig. S9 that we define our models on, all the eigenvalues $\lambda_{n,\ell}$ are shown in Supplementary Fig. S8b as functions of n and ℓ and the five solutions to Eq. (S24) with smallest $\lambda_{n,\ell}$ are plotted in the top row of Supplementary Fig. S10.



Supplementary Figure S8. **Eigenvalues of the Laplace-Beltrami operator.** Illustration of how to find $k_{n,\ell}$ and the resulting eigenvalues $\lambda_{n,\ell}$ with 896 sites of the $\{8, 3\}$ lattice shown in Fig. S9a. **a**, The function $k \mapsto g_{k,\ell}(R)$ for $\ell = 0$ (blue) and $\ell = 1$ (orange) and with $R = 0.991437$ chosen as illustrated in Fig. S9b. The first few zeroes $k_{n,\ell}$ are marked by vertical lines. **b**, The first 896 eigenvalues $\lambda_{n,\ell}$ as a function of $|\ell|$ with the different branches corresponding to different n .

A function $v(z)$ on \mathbb{D}_R can then be decomposed into the eigenfunctions $u_{n,\ell}(z)$:

$$v(z) = \sum_{n>0} \sum_{\ell \in \mathbb{Z}} v_{n,\ell} u_{n,\ell}(z), \quad (\text{S29a})$$

$$v_{n\ell} = \langle u_{n,\ell}, v \rangle = \int_{|z| \leq R} \frac{d^2z}{(1-|z|^2)^2} u_{n,\ell}(z)^* v(z). \quad (\text{S29b})$$

In Eq. (S25) we recognize that ℓ can be interpreted as angular momentum. If $v(z)$ is normalizable, $\|v\| < \infty$,

$$v_\ell = \sum_{n>0} |v_{n,\ell}|^2 \quad (\text{S30})$$

gives the contributions of different values of angular momentum ℓ to the function $v(z)$.

This can be used to find the contributions of angular momenta to quantities (vectors) defined on the lattice, e.g., the eigenstates of the Hamiltonian $\mathcal{H}_{\{8,3\}}^{\text{flake}}$ defined on a flake of the $\{8, 3\}$ lattice. A normalized vector $|\phi\rangle = (\phi_1, \dots, \phi_N)^\top$ defined on the lattice given by the finite set of sites $\{z_i\}_{i=1}^N$ induces the following function on \mathbb{D}_R

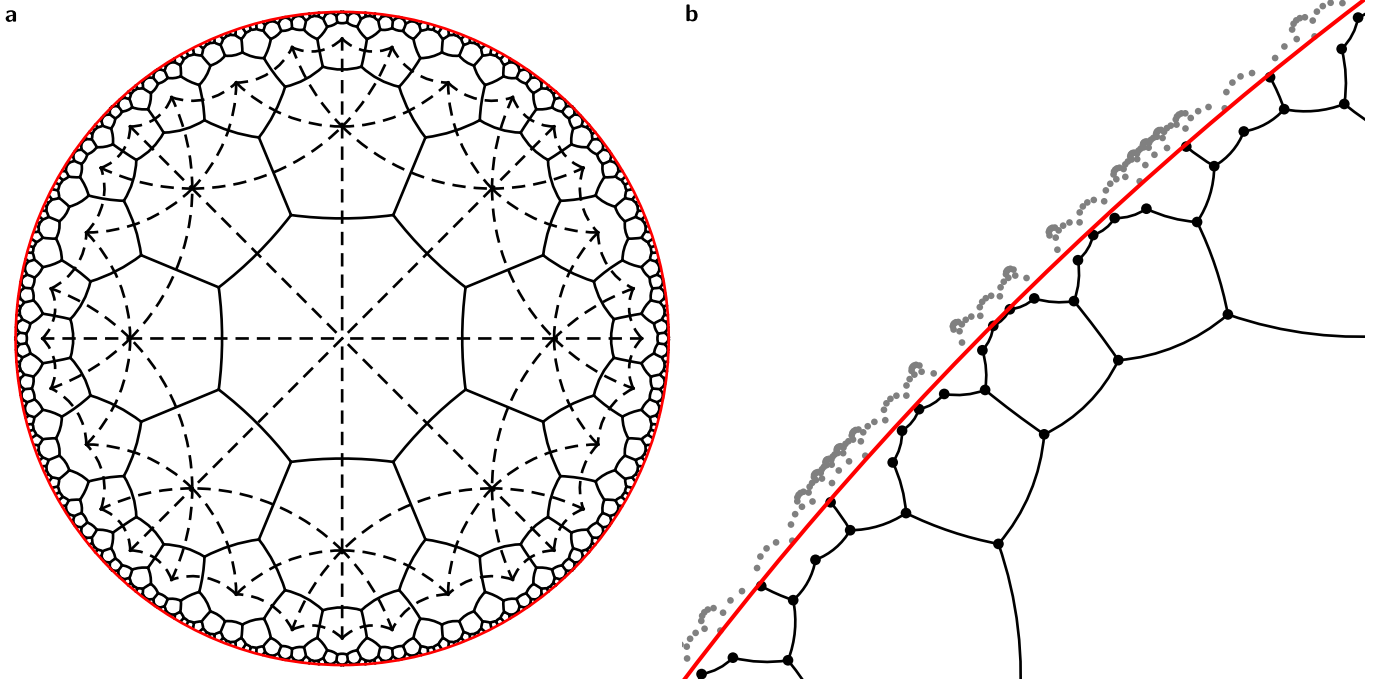
$$\phi^{(\alpha)}(z) = \sum_{i=1}^N \phi_i \eta_i^{(\alpha)}(z), \quad (\text{S31})$$

where $\eta_i(z)$ is non-vanishing only in the Wigner-Seitz cell of the lattice site i (the Wigner-Seitz cell is defined as the region of \mathbb{D}_R that has shorter hyperbolic distance to site i than to any other site of the flake), and satisfies

$$\int_{|z| \leq R} \frac{d^2z}{(1-|z|^2)^2} |\eta_i^{(\alpha)}(z)|^2 = 1. \quad (\text{S32})$$

Various choices for $\eta_i(z)$ are possible. Here we consider two options:

Option (1): $\eta_i^{(1)}(z) = \Theta_i(z) / \sqrt{A_{\text{WS}}}$, and



Supplementary Figure S9. **Flake of the $\{8, 3\}$ lattice used to extract the edge mode dispersion.** **a**, The flake with 896 sites with nearest-neighbour bonds (black lines). Some of the Wigner-Seitz unit cells are indicated by black dashed lines. The red circle bounds the disk of radius R which determines the Dirichlet boundary conditions for $u(z)$. **b**, The radius R is defined as the maximal radius r such that additional sites of the infinite hyperbolic lattice (gray points) not included in the flake (whose sites are shown with black points) lie outside the disk \mathbb{D}_r .

$$\text{Option (2): } \eta_i^{(2)}(z) = \sqrt{A_{\text{WS}}}(1 - |z_i|^2)^2 \delta^{(2)}(z - z_i).$$

In both of the above, A_{WS} is the (hyperbolic) area of a Wigner-Seitz unit cell (cf. Fig. S9); and $\Theta_i(z)$ in the first expression is a “region function” that is equal to one inside (and to zero outside) the Wigner-Seitz cell of site i . For both of the above options,

$$\langle \eta_i^{(\alpha)}, \phi^{(\alpha)} \rangle = \sum_j \phi_j \int_{|z| \leq R} \frac{d^2 z}{(1 - |z|^2)^2} [\eta_i^{(\alpha)}(z)]^* \eta_j^{(\alpha)}(z) = \phi_i \quad (\text{S33})$$

allows us get back the i^{th} component of vector $|\phi\rangle$.

The extension $\phi^{(\alpha)}(z)$ of $|\phi\rangle$ to the full disk \mathbb{D}_R allows us to apply the decomposition into eigenmodes of the Laplace-Beltrami operator given in Eq. (S29) to the vector $|\phi\rangle$:

$$\phi_{n,\ell}^{(\alpha)} = \langle u_{n,\ell}, \phi^{(\alpha)} \rangle = \sum_i \phi_i \langle u_{n,\ell}, \eta_i^{(\alpha)} \rangle. \quad (\text{S34})$$

For choice (1) this becomes

$$\phi_{n,\ell}^{(1)} = \sqrt{A_{\text{WS}}} \sum_i \phi_i \overline{u_{n,\ell}(z_i)}^* \quad (\text{S35})$$

where $\overline{u_{n,\ell}(z_i)}$ is the average over the i^{th} Wigner-Seitz cell WS_i :

$$\overline{u_{n,\ell}(z_i)} = \int_{z \in \text{WS}_i} \int_{|z| \leq R} \frac{d^2 z}{(1 - |z|^2)^2} u_{n,\ell}(z). \quad (\text{S36})$$

Choice (2) results in a much simpler expression only involving $u_{n,\ell}(z)$ evaluated at the lattice sites:

$$\phi_{n,\ell}^{(2)} = \sqrt{A_{\text{WS}}} \sum_i \phi_i u_{n,\ell}(z_i)^*. \quad (\text{S37})$$

For the two choices we define

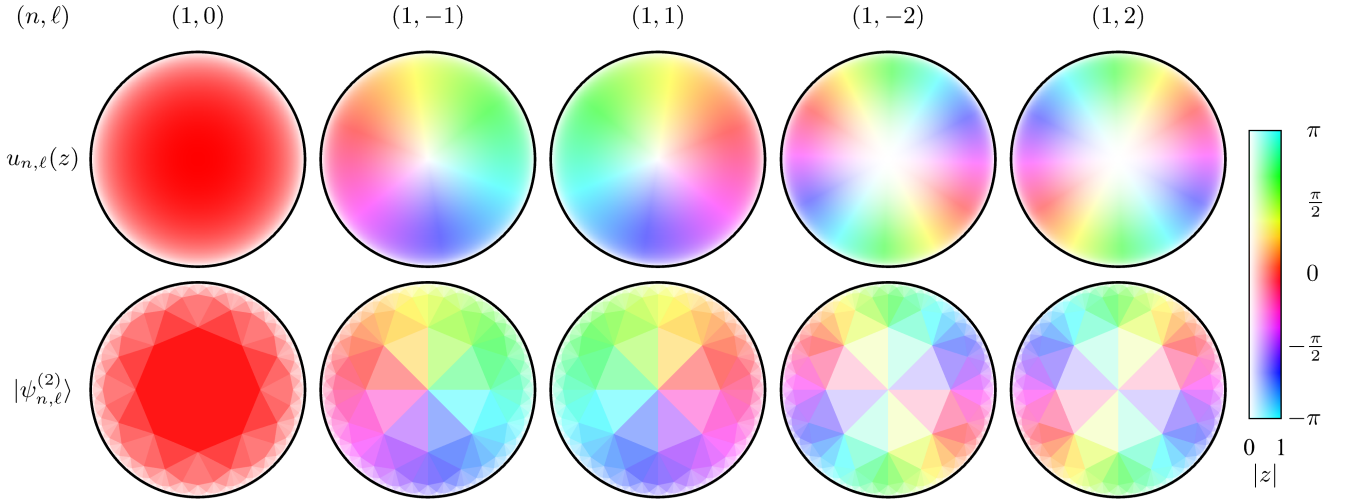
- (1): $|\psi_{n,\ell}^{(1)}\rangle = \sqrt{A_{\text{WS}}}(\overline{u_{n,\ell}(z_1)}, \dots, \overline{u_{n,\ell}(z_N)})^\top$, resp.
 (2): $|\psi_{n,\ell}^{(2)}\rangle = \sqrt{A_{\text{WS}}}(u_{n,\ell}(z_1), \dots, u_{n,\ell}(z_N))^\top$,

allowing us to express the coefficients $\phi_{n,\ell}$ compactly as

$$\phi_{n,\ell}^{(\alpha)} = \langle \psi_{n,\ell}^{(\alpha)} | \phi \rangle. \quad (\text{S38})$$

Some examples of $|\psi_{n,\ell}^{(1)}\rangle$ are shown in the bottom row of the Supplementary Fig. S10. Finally, we define the angular-momentum components

$$\phi_\ell^{(\alpha)} = \sum_{n>0} |\phi_{n,\ell}^{(\alpha)}|^2. \quad (\text{S39})$$



Supplementary Figure S10. **Eigenmodes of the Laplace-Beltrami operator.** Examples of eigenmodes $u_{n,\ell}(z)$ (top row) of the Laplace-Beltrami operator with Dirichlet boundary conditions for $|z| = R = 0.991437$. The bottom row shows the discretized versions $|\psi_{n,\ell}^{(2)}\rangle$, i.e., $u_{n,\ell}$ evaluated at the lattice sites of the flake shown in Supplementary Fig. S9. In both rows the absolute value is encoded in the intensity and the argument in the color (see legend). The header gives the quantum numbers (n, ℓ) for each eigenmode.

Note that the discretized approximations $|\psi_{n,\ell}^{(\alpha)}\rangle$ of the Laplace-Beltrami eigenmodes $u_{n,\ell}(z)$ are *neither orthogonal nor normalized*, and therefore subsets with N elements generally do not form a basis of \mathbb{C}^N . In general, a large number of $|\psi_{n,\ell}\rangle$ are required to characterize an arbitrary state $|\phi\rangle$. Owing to the choice of $t_1 = 1 > 0$, eigenstates $|\phi\rangle$ of the flake Hamiltonian, $\mathcal{H}_{\{8,3\}}^{\text{flake}}|\phi\rangle = E|\phi\rangle$, with energy E lying towards the upper end of the energy spectrum have larger contributions $\phi_{n,\ell}$ associated to small values of $\lambda_{n,\ell}$, i.e., slowly oscillating eigenfunctions $u_{n,\ell}(z)$. It is therefore easier to determine ϕ_ℓ for those states, while states with smaller energy E are highly oscillatory and require larger $|\ell|$ as well as n .

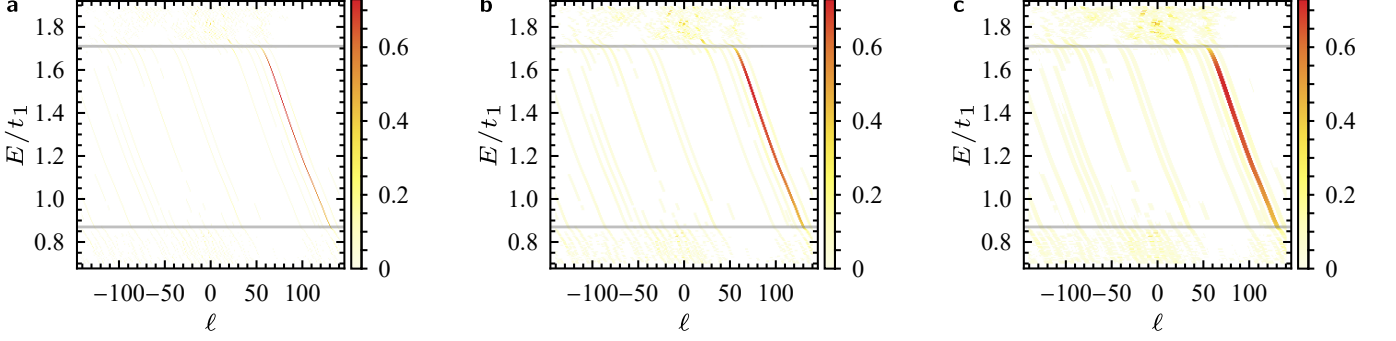
In practice, our algorithm for calculating the ϕ_ℓ for all states $|\phi\rangle$ is set up as follows. To avoid a computationally heavy numerical integration of the individual Wigner-Seitz cell, we choose option (2) discussed above. The vectors $\{|\psi_{n,\ell}^{(2)}\rangle\}_{n>0, \ell \in \mathbb{Z}}$ only depend on the finite lattice, i.e., the flake, and not the Hamiltonian matrix defined on it. Given a flake of the $\{8, 3\}$ lattice (and a compatible choice of bounding radius R), a subset of $\{|\psi_{n,\ell}\rangle\}_{n>0, \ell \in \mathbb{Z}}$ can be precomputed and stored. To do that, we first need to find solutions of Eq. (S28) for the chosen range of angular momentum $\ell \in [\ell_{\min}, \ell_{\max}]$; this is done by a root search in a predefined interval $k \in (0, k_{\max})$. Note that there is some freedom in choosing R due to the discretization; it must lie beyond the outermost site appearing on our disk-shaped flake (i.e., inside the restricted list L_{sites}), but closer than the nearest site of the $\{8, 3\}$ lattice not included in the flake (i.e., not appearing in the slightly larger list \tilde{L}_{sites}). For the system size considered here, we choose $R = 0.991437$. The resulting values $k_{n,\ell}$ allow us to define the corresponding eigenfunctions $u_{n,\ell}(z)$ via Eq. (S25) and consequently compute $|\psi_{n,\ell}^{(2)}\rangle$. Later, the overlaps $\phi_{n,\ell}^{(2)} = \langle \psi_{n,\ell}^{(2)} | \phi \rangle$ can be efficiently computed for all $|\phi\rangle$, resulting in the energy vs. angular momentum spectrum.

The results of applying the outlined algorithm to states in (and near) the upper energy gap of the hH model and of the rhKM model are shown, respectively, in the two panels of Fig. S7. Let us remark that in the main text Fig. 4(a) we plot essentially the same data as in Supplementary Fig. S7(a). However, as shown in the version of the plot in the supplementary figure, the

extracted data are very sharp (one pixel-in- ℓ wide), which would make them hard to see in the small figure panel in the main text. For this reason, we opt in the main text to coarse grain the signal in angular momentum over $(2n_{\max} + 1)$ values of angular momenta as

$$\phi_{\ell}^{(\alpha)} \mapsto \sum_{a=-n_{\max}}^{+n_{\max}} \phi_{\ell+a}^{(\alpha)}. \quad (\text{S40})$$

to improve the visibility. The result of this coarse graining for $n_{\max} \in \{0, 1, 2\}$ (i.e., over 1, 3, resp. 5 adjacent values of ℓ) is shown in Supplementary Fig. S11. The data in main text Fig. 4(a) correspond to $n_{\max} = 2$.



Supplementary Figure S11. **Smearing of chiral edge states of the hH model.** **a**, The extracted values of ϕ_{ℓ} for the chiral edge states of the hH model. **b**, The result of smearing the values shown in panel a according to Eq. (S40) with $n_{\max} = 1$ and **c** with $n_{\max} = 2$.

Supplementary Note S14: Group velocity of the chiral edge states in hyperbolic Haldane model

In this supplementary note, we show how the data in Fig. 4(a) and in Fig. 4(b) provide two independent ways to extract the velocity with which the wave packets of topological edge states in the hH model propagate around the flake boundary, allowing for a consistency check of the numerical modelling. We remark that the two figure panels are generated for *different system sizes*; therefore, one should be careful to compare absolute (rather than angular) velocities. Furthermore, the focus is not on quantitative rigor but on qualitative comparison; therefore, we approximate most of the discussed quantities to two significant digits.

We begin with Fig. 4(a), which is computed for a system with $n_{\text{sites}} = 896$, such that the number of Bolza cells is approximately $N_{\text{UC}} = 896/16 = 56$. From Eq. (S11) (where we approximate the numerator on the right-hand side by 1) we obtain for the radius R that $1 - R^2 \approx 1/56$. Next, from Eq. (S5) we obtain the perimeter $p \approx 112\pi \approx 350$. We further estimate the angular group velocity as $\omega_{\text{group}} = \Delta E / \Delta \ell$. We read from the data in Fig. 4(a) that across the energy gap $\Delta E \approx 0.83$ and $\Delta \ell \approx 65$, leading to $\omega_{\text{group}} \approx 0.0128$. Multiplying by the perimeter, we obtain the absolute group velocity $v_{\text{group}} \approx \omega_{\text{group}} p \approx 4.5$. (Here, units of length are such that the Gaussian curvature is $K = -4$, cf. Methods. Time is measured in units of \hbar/t_1 ; in numerical modelling we set both \hbar and t_1 to 1.)

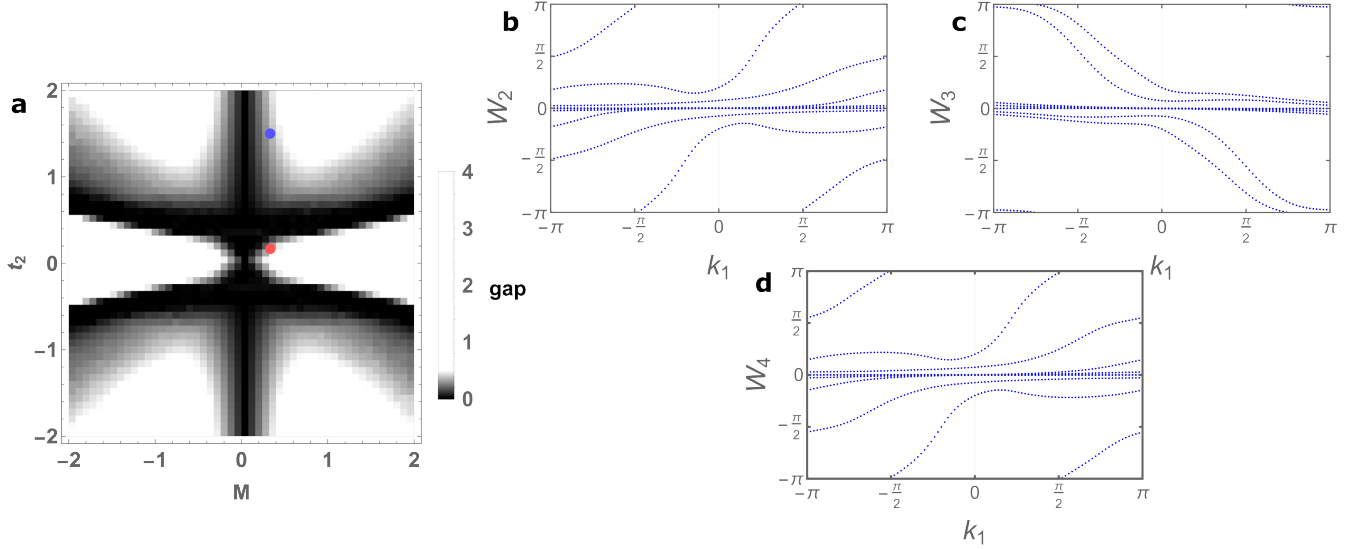
On the other hand, the data in Fig. 4(b) are obtained for a system with $n_{\text{sites}} = 1864$. Repeating analogous geometric considerations as above, we find that $N_{\text{UC}} = 116.5$, and $1 - R^2 \approx 2/233$. The perimeter of the corresponding system is estimated as $p \approx 233\pi \approx 732$. We read from the data in Fig. 4(b) that the wave packet traverses angular distance $\Delta \alpha \approx 7.5\pi$ in time $\Delta \tau = 4000$, implying angular velocity $\omega = \Delta \alpha / \Delta \tau \approx 0.0059$. Multiplying with the perimeter, we obtain the absolute speed of the wave packet propagation $v = \omega p \approx 4.3$.

We find that the two extracted values of the velocity with which the wave packets propagate along the boundary differ by $\sim 5\%$. This is acceptable agreement within our margin of error, given that several of the discussed quantities (proper choice of R , as well as intervals $\Delta \ell$ and $\Delta \alpha$) can only be extracted up to a few-percent confidence interval.

Supplementary Note S15: Phase diagram of the hyperbolic Haldane Bloch Hamiltonian at half-filling and $\Phi = \pi/2$

Recall that for the original Haldane model on the Euclidean honeycomb lattice [30], the inclusion of M drives a trivial energy gap while it is the inclusion of t_2 (at finite flux) that drives the topological gap. The boundary between the trivial and the topological insulating phases is given by the analytic formula $|M/t_2| = 3\sqrt{3}|\sin\Phi|$. In particular, the topological phase of the Euclidean Haldane model persists when M is set to zero.

In this Supplementary Note, we briefly investigate whether a similar competition between the M -driven trivial gap and the t_2 -driven topological gap also occurs at the half-filling for the hyperbolic Haldane Hamiltonian. To that end, we numerically determine [60] the energy gap at half-filling as a function of (M, t_2) for fixed values $t_1 = 1$ and $\Phi = \pi/2$. The result of this analysis is plotted in Supplementary Fig. S12(a), where the red dot indicates the value of model parameters considered throughout the manuscript.



Supplementary Figure S12. **Energy gap of the hyperbolic Haldane Bloch Hamiltonian at half-filling.** **a** We set $t_1 = 1$ and $\Phi = \pi/2$, while keeping the parameters M and t_2 variable. Shades of gray indicate the bulk energy gap of the hyperbolic Haldane model as determined by the hyperbolic band theory. Bright tones indicate large values of the gap (expressed in multiples of $t_1 = 1$), while saturated black corresponds to gap closing. Red dot at $M = 1/3$ and $t_2 = 1/6$ corresponds to the choice of parameters considered throughout the manuscript, where the energy gap at half-filling is trivial. The blue dot at $M = 1/3$ and $t_2 = 3/2$ corresponds to the parameters briefly discussed in Supplementary Note S15, where the energy gap at half-filling is associated with non-vanishing Chern numbers C_a, C_b, C_c . **b–d** Wilson-loop spectra for $M = 1/3$ and $t_2 = 3/2$ (blue dot in panel **a**), which indicate $C_a = +2$, $C_b = -2$, and $C_c = +2$.

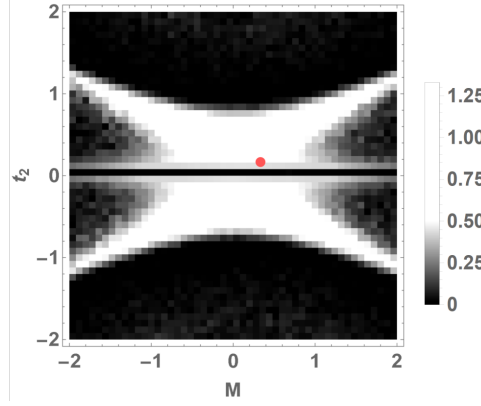
The first striking feature we observe in Supplementary Fig. S12(a) is that the hyperbolic Haldane model at half-filling, in contrast with the Euclidean one [30], is *gapless* for $M = 0$. We further observe, in resemblance with the Euclidean case, that besides the insulating phase at small values of $|t_2/M|$ there are additional gapped regions occurring at large values of $|t_2/M|$. To determine the band topology of these additional insulating phases, we fix $M = 1/3$ and $t_2 = 3/2$, which correspond to the blue dot in Supplementary Fig. S12(a). We apply the Wilson-loop technique to compute the values of Chern numbers $C_{a,b,c}$ in the insulating phase that occurs at large and *positive* t_2/M . The results of our analysis, plotted in Supplementary Fig. S12(b–d), imply $C_a = +2$, $C_b = -2$, and $C_c = +2$ i.e., the energy gap that occurs at half filling for large t_2/M is topologically non-trivial. Note, however, that the even value of the invariant implies that the corresponding rhKM model for this choice of parameters exhibits trivial values of the \mathbb{Z}_2 -valued invariants ν_a and ν_b . For large and *negative* t_2/M , the signs of the Chern numbers $C_{a,b,c}$ are flipped. We also verified that the second Chern number for these insulating regions is trivial.

Finally, we check that, in contrast to the half-filled case, the bulk energy gap at fillings $f \in \{\frac{5}{16}, \frac{11}{16}\}$ (which correspond to the Chern insulating phases studied in the main text) do not close for $M = 0$. This is illustrated explicitly for $f = \frac{5}{16}$ in Fig. S13 (with the data for $f = \frac{11}{16}$ looking essentially identical). Note that at $M = 0$ the hyperbolic Haldane model acquires an additional symmetry, namely rotation by $\pi/4$ around the center of the Bolza cell, which permutes momenta as $k_1 \mapsto k_2 \mapsto k_3 \mapsto k_4 \mapsto -k_1$. This symmetry implies that at $M = 0$ (and also for all gapped phases at finite M that extend to $M = 0$) we have

$$C_a := C_{12} = C_{23} = C_{34} = C_{14} =: C_c, \quad (\text{S41})$$

reducing the number of independent Chern numbers to two. [Let us remark that the remaining two Chern numbers could potentially be related by the three-fold rotation around a vertex of the $\{8, 3\}$ lattice. However, as this symmetry is known to act

non-orthogonally on the four momentum components [9], we leave a careful investigation of this symmetry for a future study.]



Supplementary Figure S13. **Energy gap of the hyperbolic Haldane Bloch Hamiltonian at filling $f = 5/16$.** Two gapped regions can be identified. These regions are related by a sign flip $t_2 \mapsto -t_2$. Since the same change can be interpreted as the action of time-reversal (complex conjugation flips $\Phi \mapsto -\Phi$, which at $\Phi = \pi/2$ corresponds to a sign flip of the purely imaginary t_2 term), the two gapped regions must exhibit opposite sign of all Chern numbers. The red dot indicates the parameter values $t_2 = \frac{M}{2} = \frac{1}{3}$ which are assumed throughout the main text. Since the gapped phase extends to $M = 0$, it follows from an additional $(\pi/4)$ -rotation symmetry that necessarily $C_a = C_c$, cf. Eq. (S41).